Position-Based Visual Servoing Control for Multi-Joint Hydraulic Manipulator

Shizhao Zhou[1,2,3] · Chong Shen[3] · Fengye Pang[3] · Zheng Chen[1,2,3] ⦿ · Jason Gu[4,5] · Shiqiang Zhu[3,5]

Abstract

Manipulators are widely used in various fields of industrial automation, and hydraulic manipulators have more extensive application in future by virtue of high power to weight ratio. However, compared with the traditional motor manipulators, the dynamic model of hydraulic manipulator is more complex such as higher model order characteristics, which makes the design of precision motion controller of hydraulic manipulators more challenging. In addition, the application demand of hydraulic manipulator is gradually increasing even under various harsh conditions or extreme environments, which puts forward higher requirements for the autonomous environmental perception ability of hydraulic manipulators. Therefore, the visual servoing control for hydraulic manipulator is of great research value. In this paper, a position-based visual servoing control method for multi-joint hydraulic manipulator is proposed. To be specific, based on the obtained target position, the discrete desired path points can be got by velocity-limited path interpolation, which will be transformed into a discrete sequence of desired joint angles according to well-constrained inverse kinematics. Then the continuous desired angle trajectory of manipulator joint is generated by B-spline trajectory planner. Finally, the ideal angle trajectory is input into backstepping controller to contrive the angle tracking of each joint, so as to realize the visual target following control of multi-joint hydraulic manipulator.

Keywords PBVS · eye-in-hand · Trajectory planning · Visual servo · Backstepping control

1 Introduction

As the main working tool in the field of industrial automation, manipulators are widely used in various occasions, such as factory production, assembly line processing, etc [1, 2]. In recent years, due to the progress of science and technology and the continuous development of human society, the application demand of manipulators has been gradually increasing, even in various harsh conditions or extreme environments (underwater detection, explosive disposal, disaster area exploration, etc.) [3]. As an important branch of manipulator, hydraulic manipulator is very practical in these extreme environments because of its high power to weight ratio. However, currently, most multi-joint hydraulic manipulators are operated by offline programs designed for given tasks or through manual remote controls

for flexibility. These operation modes cannot make timely adjustments independently when the operation target deviates from the command position or when the operation target moves, which greatly reduces the practical value of such hydraulic manipulators [4, 5]. Therefore, how to enhance the complex operation ability of hydraulic manipulator in unstructured environment, realizing the external environment perception of hydraulic manipulator and the function of autonomously planning operation path are urgent problems to be solved [6, 7].

The installation of external sensors can effectively improve the ability of hydraulic manipulators to perceive the external working environment and thus improve their autonomous operation ability [8, 9]. Currently, industrial manipulators are usually equipped with position sensors. [10] However, as the working environment becomes more and more complex, only relying on position sensors becomes insufficient for fully perceiving the external environment. [11, 12] Visual servo control systems, which feedback the visual information obtained by visual sensors to the controller, thereby ensure that a manipulator achieves its desired position and orientation under the guidance of the camera. Developing

✉ Zheng Chen
  zheng_chen@zju.edu.cn

Extended author information available on the last page of the article.

such systems has therefore gradually become a research focus [13, 14].

The current visual servo system of a manipulator can be divided into two categories according to the position where the camera is installed [15]: one is eye-in-hand configuration, in which the camera is fixed on the end-effector of manipulator and moves with the manipulator simultaneously [16]; another is eye-to-hand configuration, in which the relative position between camera and manipulator base is constant and the camera cannot move. The eye-in-hand visual system transmits the distance between target object and the end-effector of manipulator to the controller obtained by the camera as servo signals, thus realizing visual servo control, while it is the target position information that is obtained and transmitted in eye-to-hand system [17]. On the one hand, for eye-in-hand configuration, the target object sometimes exceeds the field of view of the camera and thus causes the target to be lost for the reason that the field of view of the system is time-varying and generally small. On the other hand, although it is not easy to lose the visual target for eye-to-hand configuration for its relatively large viewing range, there are other problems in eye-to-hand system such as the manipulator obstructing target object during the movement and large measurement error when the manipulator or the visual target are far away from camera. Another method is to classify the visual servo system by the feedback signals [18]. The method of realizing the servo control by feedbacking position signals is called PBVS. The given expected position and feedback signals under PBVS are defined in Cartesian space, and the motion path of the manipulator can be planned directly in 3D space, so the singular problems and local minimum problem can be avoided, while control performance of PBVS is sensitive to kinematics modeling error and camera parameter calibration error [19]. The method of manipulator servo control by image feedback signal is called IBVS, which does not need to estimate the relative position from the end-effector to target object [20]. Thus, IBVS method has strong robustness on error of camera parameters, dynamic modeling error and image measurement error [21]. However, the image Jacobian matrix singularity or local minimum problems may occur, resulting in a steady-state error in image space and actual position.

There are many researches on the visual servo control of traditional electric industrial manipulators so far. Among these researches, Bae et al. proposed a dynamic visual servo controller, which implements an image-based visual servo method for electric manipulators in joint space by using a dual-loop control structure [22]. Burger et al. proposed a second-order sliding mode controller based on position-based visual servo, which enables the robot to follow the target by controlling the position and direction of end-effector and handling the problem of large initial error [23]. Hwang et al. developed an IBVS algorithm based on deep learning, and verified its advantage in processing speed by simulation [24]. Zhang et al. designed a visual servo system combined with a neural network, which improves the security in the visual servo process and verifies its validity under the simulation conditions [25]. Wang et al. implemented PBVS on a three-joint electric manipulator and achieved an end position control error of 1 mm for the stationary target [26].

However, the above visual servo control methods are based on the traditional electric manipulator platform, meanwhile the visual servo control for the hydraulic manipulator is more difficult than the traditional electromechanical arm [27–29]. Firstly, the dynamic model of the hydraulic manipulator has higher order, for the reason that the third order dynamics consisting of robotic dynamics and the chamber pressure as well as the hydraulic dynamics need to be considered in the motion control [30–32]. Secondly, valve-controlled hydraulic actuators are often affected by non-linear factors such as non-linear pressure-flow gain, discontinuity due to valve switching, and external disturbances, and thus the design of hydraulic manipulator controller is more challenging than traditional electric manipulator [33–35]. Due to the forementioned problems, only a few studies have been done on implementing visual servo control on hydraulic system [36, 37]. Sivcev et al. presents a position-based visual servo control method for underwater hydraulic manipulator based on monocular camera and autonomous grabbing operation [38]. However, this visual servo control method only considers the kinematics of the manipulator but does not carry out dynamic control research. With the requirement on autonomy of the hydraulic manipulator operation and the increasing complexity of the operation scene, how to achieve the visual servo control of the hydraulic manipulator considering the high-order non-linear dynamics of the hydraulic manipulator and overcoming the presence of a variety of external disturbances is of great practical significance [39].

In this paper, a position-based visual servoing control method is proposed for multi-joint hydraulic manipulator. Firstly, besides the kinematics model, the high-order dynamic model is established according to robotic dynamics and hydraulic dynamics. Besides, because the hydraulic manipulator usually works in harsh or extreme environment, this paper adopts eye-in-hand visual servo system, and PBVS method is used to recognize the visual target and generate servo signals. The B-spline programming method is used to obtain the third order differentiable joint angle trajectory of the manipulator, which is smooth enough

to meet the requirements of controller designed. Based on the planning trajectory and the higher-order dynamics model, the backstepping controller is designed to cope with the issues such as the uncertain nonlinear and external disturbances, which can achieve the good control performance in the joint space, while realize the visual servo function of the hydraulic manipulator.

The remaining of this paper is organized as follows. Section 2 describes the kinematic model and dynamic model of the hydraulic manipulator. Section 3 introduces the visual servo system designed in this paper, including target recognition, speed limited interpolation and trajectory planning, by which the image is proposed and a desired joint angle trajectory is generated. Section 4 establishes a determined robust controller based on the high-order nonlinear dynamic model of the hydraulic manipulator. Section 5 proposes the experimental setup and result to test the performance of the designed hydraulic manipulator visual servoing control system.

$$
{}^{i}T_{i+1} = \begin{bmatrix} \cos q_{i+1} & -\sin q_{i+1}\cos\alpha_{i+1} & \sin q_{i+1}\sin\alpha_{i+1} & a_{i+1}\cos q_{i+1} \\ \sin q_{i+1} & \cos q_{i+1}\cos\alpha_{i+1} & -\cos q_{i+1}\sin\alpha_{i+1} & a_{i+1}\sin q_{i+1} \\ 0 & \sin\alpha_{i+1} & \cos\alpha_{i+1} & d_{i+1} \\ 0 & 0 & 0 & 1 \end{bmatrix} \tag{1}
$$

where ${}^{i}T_{i+1}$ means the transformation matrix between the coordinates rigidly attached to i-th joint and (i+1)-th joint. q_{i+1} is rotation angle of (i+1)-th joint. a_{i+1}, α_{i+1}, d_{i+1} are i-th link length, link twist, link offset. By multiplying the transformation matrices successively, we get the transformation matrix between base and grasper (manipulator base is regarded as the 0-th joint):

$$
{}^{base}T_{grasper} = {}^{0}T_{5} = \prod_{i=0}^{4} {}^{i}T_{i+1} \tag{2}
$$

For the eye-in-hand camera installation method illustrated in Fig. 2, with the mounting position of camera is calibratable and a Cartesian coordinate is selected and rigidly attached to camera, another homogeneous transformation matrix is given as follows:

$$
{}^{4}T_{camera} = \begin{bmatrix} 1 & 0 & 0 & d_{camera} \\ 0 & 1 & 0 & 0 \\ 0 & 0 & 1 & h_{camera} \\ 0 & 0 & 0 & 1 \end{bmatrix} \tag{3}
$$

Where the d_{cam}, h_{cam} is the camera mounting position. So the transformation matrix between base and camera ${}^{base}T_{cam}$ is obtained.

$$
{}^{base}T_{camera} = \left(\prod_{i=0}^{3} {}^{i}T_{i+1} \right) {}^{4}T_{camera} \tag{4}
$$

2 Modelling and Problem Formulation

The goal of this paper is developing a PBVS system with eye-in-hand configuration applied to multi-joint hydraulic manipulator. In consideration of the proposed method generalizability, the most common articulated hydraulic manipulator is illustrated in Fig. 1. As for the visual servoing equipment, the camera is attached to the place beside end-effector (that is a gripper in our experiment for example), which obeys the eye-in-hand configuration .

2.1 Manipulator-Camera System Kinematics

If the structural parameters of manipulator are well known, it would be convenient to establish the kinematics model in virtue of the Denavit-Hartenberg (hereinafter referred as D-H) convention. Specifically, for articulated manipulator with n-DoF, a homogeneous transformation matrix relating each two adjacent joint coordinates can be written as follows:

In order to guide the manipulator grasper approaching target object, it is necessary to obtain the target position by processing captured RGB-D picture. Once the target center position in image coordinates $\left[u_{t\,arg\,et}, v_{t\,arg\,et}\right]$ is got, relative direction of the target is obtained. Then, combining the distance of target object $d_{t\,arg\,et}$ extracted from the depth picture, the target position relative to the camera can be figured out:

$$
\begin{bmatrix} {}^{camera}x_{target} \\ {}^{camera}y_{target} \\ {}^{camera}z_{target} \end{bmatrix} = \frac{d_{target}}{\sqrt{u_{target}^2 + v_{target}^2 + 1}} K^{-1} \begin{bmatrix} u_{target} \\ v_{target} \\ 1 \end{bmatrix} \tag{5}
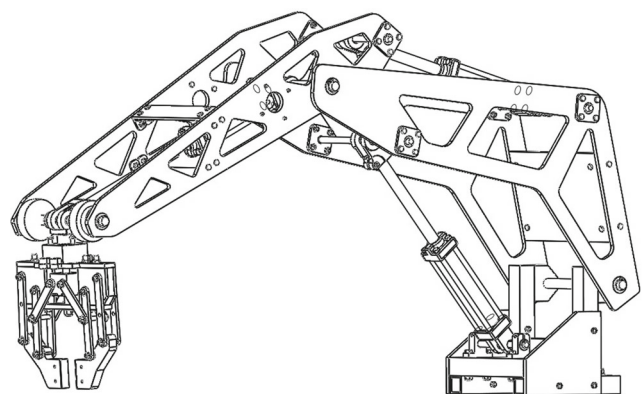$$

Fig. 1 Common Articulated Hydraulic Manipulator
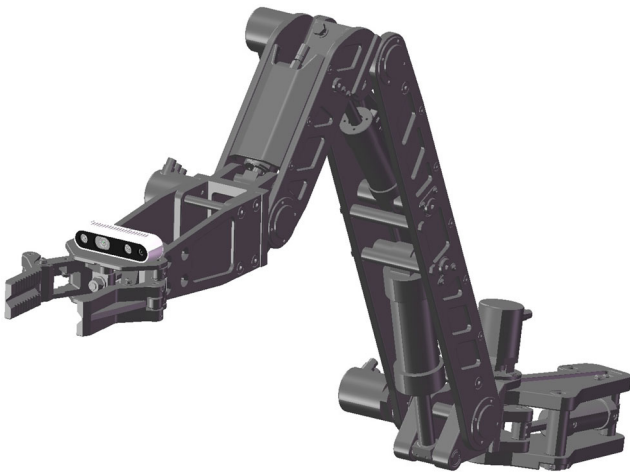
Fig. 2 Eye-in-hand Visual Servoing Configuration

where the K is the internal parameter matrix obtained by calibration. So the transformation matrix between camera and target would be:

$$^{camera}T_{target} = \begin{bmatrix} 1 & 0 & 0 & ^{camera}x_{target} \\ 0 & 1 & 0 & ^{camera}y_{target} \\ 0 & 0 & 1 & ^{camera}z_{target} \\ 0 & 0 & 0 & 1 \end{bmatrix} \quad (6)$$

By multiplying $^{camera}T_{target}$ by $^{base}T_{camera}$, the transformation matrix between base and target $^{base}T_{target}$ is obtained:

$$^{base}T_{target} = {}^{base}T_{camera} \cdot {}^{camera}T_{target} \quad (7)$$

After all these steps, the manipulator-camera system kinematics has been completely modelled, and will be the foundation of trajectory plan function realization in Section 4.

2.2 Hydraulic Manipulator Dynamics

The dynamic model of n-DoF hydraulic manipulator in joint space is given as

$$\begin{aligned} &M_j(q)\ddot{q} + C_j(q,\dot{q})\dot{q} + G_j(q) \\ &= u_j + D_j(q,\dot{q}) + \Delta_j(q,\dot{q},t) \end{aligned} \quad (8)$$

where $q \in R^n$, $\dot{q} \in R^n$ and $\ddot{q} \in R^n$ represent the joint position, velocities and accelerations, respectively. $u_j \in R^n$ is the equivalent control input. $M_j(q) \in R^{n \times n}$, $C_j(q,\dot{q})\dot{q} \in R^n$ and $G_j(q) \in R^n$ represent the symmetric positive definite manipulator inertia matrix, the centripetal and Coriolis torque, and the gravitational torque, respectively. $D_j(q,\dot{q})$ is the disturbance torque which concludes the joint friction torque and friction of hydraulic system. All the uncertain nonlinearities can be lumped into $\Delta_j(q,\dot{q},t) \in R^n$.

Equation 8 have the following properties [23]:

Property I   In any finite work space, $M_j(q)$ is symmetric positive definite matrixes with:

$$\alpha_{min}I \le M_j(q) \le \alpha_{max}I \quad (9)$$

where α_{min} and α_{max} are positive scalars.

Property II   The matrixes $\dot{M}_j(q) - 2C_j(q,\dot{q})$ is skew-symmetric.

Property III   According to the selection of appropriate manipulator and target parameter set, the dynamic equation can be expressed as linear which is shown as:

$$M_j(q)\ddot{q} + C_c(q,\dot{q})\dot{q} + G_c(q) = \varphi(q,\dot{q})^T\theta \quad (10)$$

where θ is the manipulator parameters, $\varphi(q,\dot{q})^T$ is the regressor matrixes.

Property IV   The bounds of uncertain nonlinearities are known and can be expressed as follow:

$$|\Delta_j| \le \delta \quad (11)$$

where δ is known constant scalars.

Different from the traditional electric drive machinery, the equivalent control input of the hydraulic manipulator can be expressed as:

$$u_j = J_j(q)^T(P_iA_i - P_oA_o) \quad (12)$$

where $P_i \in R^n$ and $P_o \in R^n$ represent the pressure in the oil inlet and return chamber of joint hydraulic cylinder, respectively. $A_i \in R^n$ and $A_o \in R^n$ represents the contact area of joint hydraulic cylinder push rod in the oil inlet and return chamber, respectively. $l \in R^n$ is the rod extension of joint hydraulic chamber. $J_j(q) = \frac{\partial l(q)}{\partial q} \in R^{n \times n}$ is the nonsingular Jacobian matrix which can be written as:

$$J_j(q) = \begin{bmatrix} \frac{\partial l_1}{\partial q_1} & \frac{\partial l_1}{\partial q_2} & \cdots & \frac{\partial l_1}{\partial q_n} \\ \frac{\partial l_2}{\partial q_1} & \frac{\partial l_2}{\partial q_2} & \cdots & \frac{\partial l_2}{\partial q_n} \\ \cdots & \cdots & \cdots & \cdots \\ \frac{\partial l_n}{\partial q_1} & \frac{\partial l_n}{\partial q_2} & \cdots & \frac{\partial l_n}{\partial q_n} \end{bmatrix} \quad (13)$$

The driving system of common n-joint hydraulic manipulator is shown in Fig. 3.

Assuming no leakage of chamber, the dynamic of hydraulic drive cylinder which is clarified as Fig. 4 can be written as follows:

$$V_i\dot{P}_i\beta_e^{-1} = -A_iJ_j(q)^T\dot{q} + Q_i \quad (14)$$

$$V_o\dot{P}_o\beta_e^{-1} = A_oJ_j(q)^T\dot{q} - Q_o \quad (15)$$

where $V_i = V_{hi} + A_il \in R^n$ and $V_o = V_{ho} - A_ol \in R^n$ represents the volume of oil inlet and return chamber of hydraulic cylinder, respectively. $V_{hi} \in R^n$ and $V_{ho} \in R^n$ the volume of the inlet and return chamber in the initial case ($l = 0$) respectively. So far, the equivalent control input u has been converted into flow input Q_i and Q_o.

Fig. 3 Multi Joint Hydraulic Manipulator Driving System
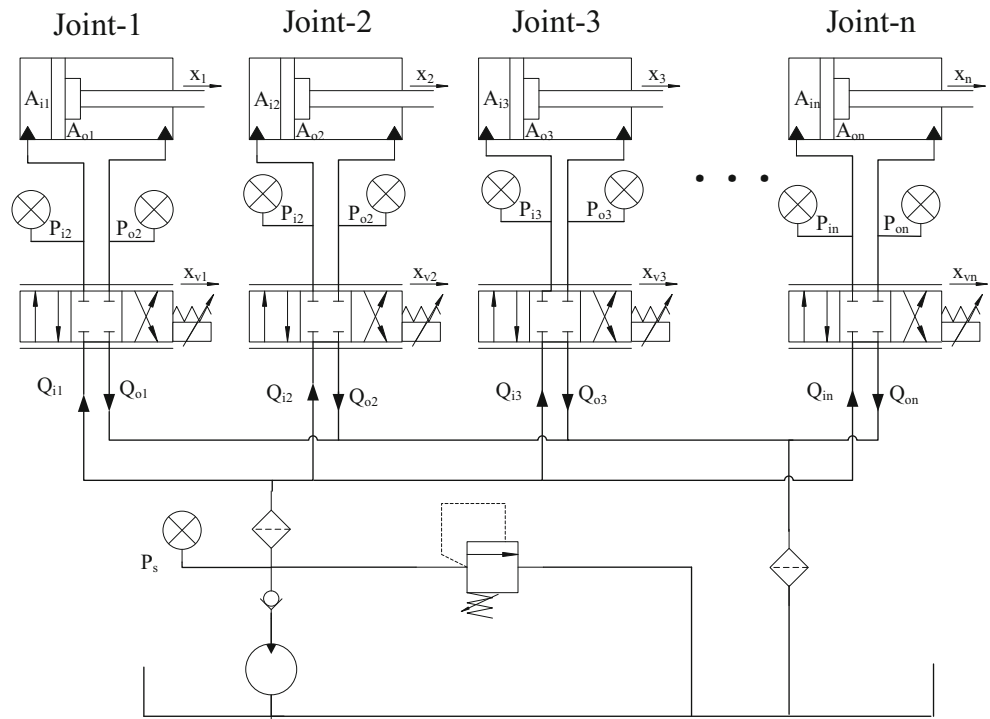
Besides, the flow input can be further written as:

$$Q_i = k_{qi} g_i(P_i, x_v) x_v \tag{16}$$

$$Q_o = k_{qo} g_o(P_o, x_v) x_v \tag{17}$$

where $x_v \in R^n$ is the displacement of joint valve spool. $k_{qi} \in R^n$ and $k_{qo} \in R^n$ is the gain parameter of flow. $g_i(P_i, x_v) \in R^n$ and $g_o(P_o, x_v) \in R^n$ can be written as:

$$g_i(P_i, x_v) = \begin{cases} \sqrt{P_s - P_i} & x_v \geq 0 \\ \sqrt{P_i - P_r} & x_v < 0 \end{cases} \tag{18}$$

$$g_o(P_o, x_v) = \begin{cases} \sqrt{P_i - P_r} & x_v \geq 0 \\ \sqrt{P_s - P_i} & x_v < 0 \end{cases} \tag{19}$$

where P_s is the supply pressure of the hydraulic pump, and P_r is the reference pressure of the hydraulic oil-return system.
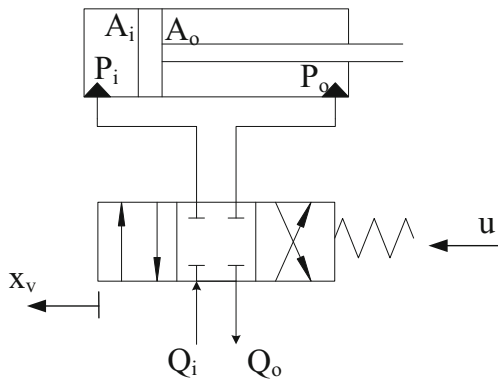

Fig. 4 Hydraulic Cylinder Driven System

In the actual hydraulic control system, the displacement of valve spool can be adjusted by change the input voltage of hydraulic valve such as:

$$x_v = f(U_c) \tag{20}$$

Hence, the equivalent control input u_j has been converted into the controllable input voltage.

2.3 Problem Formulation

In this paper, a position-based visual servoing system with eye-in-hand configuration is designed to determine the target position and plan an appropriate trajectory lending itself to guide the joints to approaching the target, the ultimate goal is to realize the visual target following control of multi joint hydraulic manipulator end-effector through real-time controlling the system input U_c while ensuring the system stability under the condition that the hydraulic manipulator is influenced by factors such as external interference and uncertain nonlinearity.

3 Visual Servoing System Design

The main framework of position-based visual servoing control of multi joint hydraulic manipulator proposed in this paper is shown in the Fig. 5. Firstly, based on the recognized visual target pose, the discrete desired path points are obtained through velocity-limited path interpolation. The desired path is transformed into a discrete sequence of
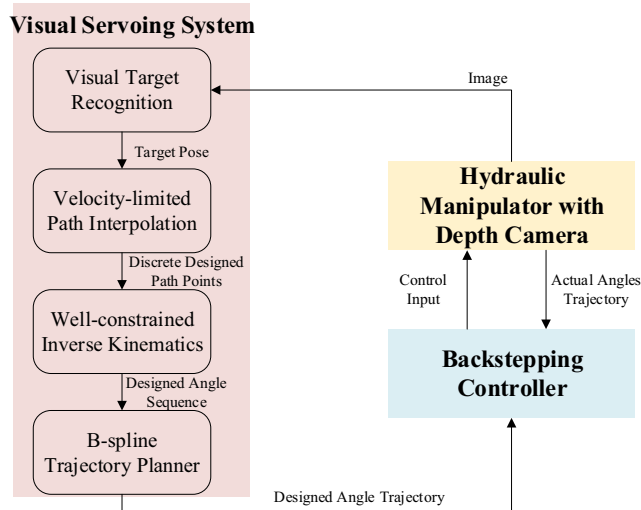
Visual Servoing System

Fig. 5 Framework of Designed Visual Servoing Control Method

Fig. 6 ArUco Marker Detection

desired angles of each joint by using well-constrained inverse kinematics, and then the desired angle trajectory of each joint is generated by B-spline trajectory planner. Finally, the ideal angle trajectory is input into backstepping controller to contrive the angle tracking of each joint, so as to realize the visual target following control of multi joint hydraulic manipulator.

3.1 Target Recognition

Because that the core focus is to convert the desired pose into high-order differentiable servo signal after visual target recognition rather than extracting the target pose from the image, and the method proposed in this paper is independent of the pose estimation algorithm, in order to reduce the cumulative error in other aspects (such as target detection), the ArUco marker in Opencv library is used as the visual target to stably obtain the position information of the target.

After the target detection is completed (as shown in Fig. 6), establish ArUco marker coordinates. According to the relative position between the camera coordinate and the ArUco mark coordinate and the relative position between the camera and the manipulator end-effector, the relative position between the visual target and the manipulator end-effector is finally obtained. It should be noted that the z-axis information is not obtained directly from the ArUco image, but is extracted from the depth map at the corresponding position of the ArUco code (the depth map mentioned here is taken by the depth camera used in the experiment), so as to keep the error of Z axis is not significantly greater than that of X and Y axes.
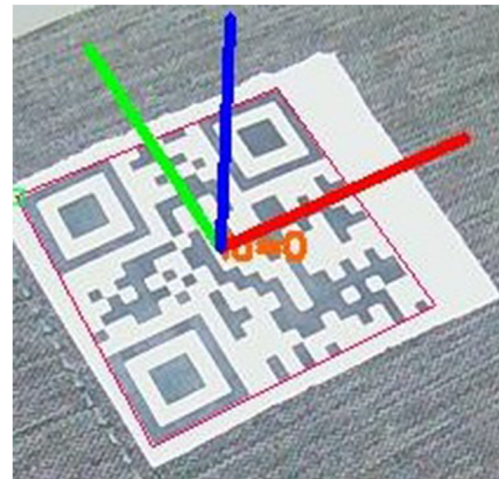
3.2 Velocity-limited Path Interpolation

By using Eq. 7, the transformation matrix between base and target can be obtained, which can be written as:

$$^{target}T_{base} = \begin{bmatrix} 1 & 0 & 0 & x_{target} \\ 0 & 1 & 0 & y_{target} \\ 0 & 0 & 1 & z_{target} \\ 0 & 0 & 0 & 1 \end{bmatrix} \quad (21)$$

Meanwhile, the transformation matrix between base and gripper can also be calculated by Eq. 2.

$$^{gripper}T_{base} = \begin{bmatrix} 1 & 0 & 0 & x_{gripper} \\ 0 & 1 & 0 & y_{gripper} \\ 0 & 0 & 1 & z_{gripper} \\ 0 & 0 & 0 & 1 \end{bmatrix} \quad (22)$$

To guide the gripper approaching to the target, we need to plan a path with appropriate orientation and velocity. Therefore, we put forward a path interpolation method as follows to generate discrete path points with constant time intervals in Cartesian space. The n-th path interpolation is expressed in general form as follows:

$$\begin{aligned} \mathbf{p}_{interp}\left(nT_{interp}\right) = {} & \mathbf{p}_{interp}\left((n-1)\,T_{interp}\right) \\ & + d_{interp}\left(nT_{interp}\right) \\ & \cdot \mathbf{e}_{interp}\left(nT_{interp}\right) \end{aligned} \quad (23)$$

where $\mathbf{p}_{interp} \triangleq \begin{bmatrix} x_{interp} & y_{interp} & z_{interp} \end{bmatrix}^T$ is the discrete sequence of path interpolation points; T_{interp} is the constant time interval of generated points; $d_{interp} \in \mathbb{R}$ is the distance between (n-1)-th and n-th interpolation points; $\mathbf{e}_{interp} \in \mathbb{R}^{3 \times 1}$ is the orientation of n-th interpolation point.

From the perspective of application scenario, movement of target and rotation of joints certainly cause the changing of $^{target}\mathbf{p}_{base}$ and $^{gripper}\mathbf{p}_{base}$, which means the direction and

distance between gripper and target are not constant nor predictable. Thus, to generate a path with right orientation and appropriate velocity, the regulation of determining interpolation distance d_{interp} and orientation $\mathbf{e}_{interp}$ is proposed as follows:

$$
\begin{cases}
d_{interp} = v_{\max} T_{interp} \cdot f\left(\frac{\|\mathbf{p}_{t\,arg\,et} - \mathbf{p}_{gripper}\|}{v_{\max} T_{interp}} \right) \\
\mathbf{e}_{interp} = \frac{\mathbf{p}_{t\,arg\,et} - \mathbf{p}_{gripper}}{\|\mathbf{p}_{t\,arg\,et} - \mathbf{p}_{gripper}\|}
\end{cases}
\tag{24}
$$

where $v_{\max}$ is the maximum of gripper velocity allowed; $f(.)$ is a function used to automatically adjust the space interval of next interpolation point according to the distance between gripper and target, which is required to be 0 when $\|\mathbf{p}_{t\,arg\,et} - \mathbf{p}_{gripper}\| = 0$ and always be no larger than 1. In experiments, the function $f(.)$ is selected as $\tanh(.)$, and there are alternative functions like sigmoid function and saturation function.

By adjusting d_{interp}, which is space interval between adjacent interpolation points, the velocity value of the planned path is also adjusted indirectly according to the distance between gripper and target, and the velocity orientation is always toward the target.

3.3 Well-Constrained Inverse Kinematics

Since the controller designed in Section 3 works in joint space, the path interpolation result $\mathbf{p}_{interp} = [x_{interp}$ $y_{interp}\ z_{interp}]^T$ should be uniquely mapped from Cartesian space into joint space $\mathbf{q}_{interp} = [q_{1interp}\ q_{2interp}\ q_{3interp}$ $q_{4interp}]^T$, and a relatively general method is using inverse kinematics. However, there is no standard method to uniquely determine the mapping result for the 4-DoF manipulator, which is insufficient for pose control (6 DoF required) while is redundant for position control (3 DoF required). Therefore, the inverse kinematics of the 4 DoF manipulator would be either an over-constrained problem or an under-constrained problem if simply applying the traditional pose control or position control criterion.

To resolve the tricky DoF number problem and propose a set of well-constrained mapping rules, inverse kinematics of position control is improved to output the unique mapping result. In addition to the 3 DoF constraints proved by position control criterion showed in Eq. 25(1,2,3), pitch angle of the manipulator gripper is regarded as another constraint in Eq. 25(4), so the transformation from Cartesian space to joint space is completely constrained and the mapping rule is well defined. Specifically, the pitch angle is required to be toward to the target, and the constraints in the improved inverse kinematics for the specific configuration of the 4 DoF articulated manipulator are summed up as follows:

$$
\begin{cases}
x_{interp} = (a_1 + a_2 C_2 + a_3 C_{23} + a_4 C_{234}) S_1 \\
y_{interp} = (a_1 + a_2 C_2 + a_3 C_{23} + a_4 C_{234}) C_1 \\
z_{interp} = a_2 S_2 + a_3 S_{23} + a_4 S_{234} \\
-\text{atan2}\left({}^{target}z_{interp}, \sqrt{{}^{target}x_{interp}^2 + {}^{target}y_{interp}^2} \right) = q_{2interp} + q_{3interp} + q_{4interp}
\end{cases}
\tag{25}
$$

where a_i, $i = 1, 2, 3, 4$ are D-H parameters representing link length; S_i, C_i, $i = 1, 2, 3, 4$ are sine and cosine of i-th element in $\mathbf{q}_{interp}$ (subscript composed of multiple numbers means the sum of corresponding elements).

By these equations the space transformation result can be figured out, so the joint angles corresponding to each path interpolation point are obtained.

$$
\begin{cases}
q_{1interp} = \text{atan2}\left(y_{interp}, x_{interp} \right) \\
q_{2interp} = \text{atan2}\left(h_{interp}, r_{interp} \right) - \arccos\left(\frac{a_2^2 + r_{interp}^2 + h_{interp}^2 - a_3^2}{2a_2\sqrt{r_{interp}^2 + h_{interp}^2}} \right) \\
q_{3interp} = 180 - \arccos\left(\frac{a_2^2 + r_{interp}^2 + h_{interp}^2 - a_3^2}{2a_2 a_3} \right) \\
q_{4interp} = -\text{atan2}\left({}^{t\,arg\,et}z_{interp}, \sqrt{{}^{t\,arg\,et}x_{interp}^2 + {}^{t\,arg\,et}y_{interp}^2} \right) - q_{2interp} - q_{3interp}
\end{cases}
\tag{26}
$$

It is worthy of note that the function atan2() is used to eliminate another solution, for the sake that the rotation ranges of joint 1,3,4 are bounded. By virtue of the rotating angle range boundary, the well-constrained inverse kinematics solution is uniquely determined by substituting arctan() by atan2(), and consequently the path interpolation in Cartesian space $\mathbf{p}_{interp}$ is transformed into discrete joint angle $\mathbf{q}_{interp}$.

3.4 B-spline-based Trajectory Planning

To provide a desired trajectory in joint space as the input of the joint controller proposed in Section 4, the discrete desired points need to be transformed into a continuous trajectory (the control frequency is set as 4kHz because that it is generally considered that the control frequency of the discrete controller should reach at least twice the hardware bandwidth to give full play to the controller, comparing to the visual servo rate, the trajectory obviously needs to be transformed into a continuous trajectory). As explained in Section 2.2, the dynamic model of hydraulic manipulator is as high as 3 order, which indicates the realization of most model-based controllers, including the backstepping controller designed in Section 4, would involve the derivative of desired joint angle trajectory in time domain whose highest order is equal to the model order. Consequently, there is a requirement that the desired joint angle trajectories generated should be third order differentiable to be a valid input of the controller designed. The existence of the third order derivative of desired joint angle in algorithm realization of the backstepping controller designed will be specifically highlighted in Section 4.

As a result, simply connecting the discrete-time angle points $\mathbf{q}_{interp}$ into polygonal line trajectory and setting velocity for every line segment would result in indifferentiable angle velocity and cannot meet the requirement. Taking the n-th interpolation for example, there are 4 requirements for potential trajectory planning methods to smooth the desired angle trajectory:

Requirement I

Input signal includes discrete points in joint space $\mathbf{q}_{interp}(nT_{interp})$ and corresponding time nT_{interp}, and output should be continuous desired angles for all joints $\mathbf{q}_d(t) = [q_{1d} \ q_{2d} \ q_{3d} \ q_{4d}]^T$;

Requirement II

For the visual servo system works in real-time condition, the plan regulation obeys causality and depends on known desired points $\mathbf{q}_{interp}(kT_{interp})$, $k < {}^t/T_{interp}$, where is the time parameter in $\mathbf{q}_d(t)$;

Requirement III

In consideration of the differentiability requirement of controller input, planned angle trajectories $\mathbf{q}_d(t)$ are required to be 3-order differentiable in time domain, namely the $\frac{\partial^3 \mathbf{q}_d}{\partial t^3}$ exists;

Requirement IV

If the discrete desired angle points $\mathbf{q}_{interp}(nT_{interp})$ converge to a certain value $\mathbf{q}_{interp}(\infty)$, the planned joint angles $\mathbf{q}_d(t)$ are required to converge to the same value in limited time.

Taking all these requirements into consideration, 4-dimensional Cubic B-spline is chosen to process the discrete-time angles. To describe the exact form of the base function of B-spline is defined by Cox-de Boor iteration as follow:

$$\begin{cases} B_{i,p}(u) = \frac{u - u_i}{u_{i+p} - u_i} B_{i,p-1}(u) + \frac{u_{i+p+1} - u}{u_{i+p+1} - u_{i+1}} B_{i+1,p-1}(u) \\ B_{i,0}(u) = \begin{cases} 1, \ u_i \le u < u_{i+1} \\ 0, \ \text{else} \end{cases} \end{cases}$$

$$(27)$$

where $B_{i,p}(u)$ means the i-th segment of p-order B-spline base function; u_i is the i-th element in the knot sequence. And the B-spline itself is defined in the parametric equation form as follow:

$$C_p(u) = \sum_{i=0}^{n} B_{i,n}(u) P_i \qquad (28)$$

where n is the length of control point sequence of B-spline; P_i is the i-th control points of B-spline, which is a series of points and every point is in the space with dimension number of B-spline. Some useful properties of B-spline can be deduced from its definition [40–42].

Property I

B-spline has parameter continuity property. For p-order B-spline, the curve is the $(p - 1)$ order parameter continuous, which means every dimension of the curve would be p-order differentiable for parameter u.

Property II

B-spline has local support property. For p-order B-spline, when $u_i \le u < u_{i+1}$, the curve value $C_p(u)$ would only depend on a part of control points: $P_i, P_{i+1}, \cdots, P_{i+p+1}$.

Property III

B-spline has conditional clamped property. For p-order B-spline, the curve would pass through the first and last control points if the first $p + 1$ and last $p + 1$ knots are the same or the first $p + 1$ and last $p + 1$ control points are repetitive.

Comprehensively utilizing the aforementioned properties of B-spline, a real-time trajectory planner based on 4-dimensional cubic B-splined is constructed as follows:

$$\mathbf{q}_d(t) = \sum_{i=0}^{3} B_{i,3}\left(\frac{t}{T_s} - i_t\right) \mathbf{q}_{interp}((i + i_t - 3)T_s) \quad (29)$$

where the $i_t = \left\lfloor \frac{t}{T_s} \right\rfloor$ and the knots are defined as $u_i = i$. So the trajectory expressed as Eq. 29 is a third order B-spline whose i_t-th segment is constructed with $\left(\frac{t}{T_s} - i_t\right)$ as base function parameter and with $\mathbf{q}_d((i_t - 3)T_s)$, $\mathbf{q}_d((i_t - 2)T_s)$, $\mathbf{q}_d((i_t - 1)T_s)$, $\mathbf{q}_d(i_t T_s)$ as control points. According to the properties 1-3, it can be concluded that the 4-dimensional cubic B-spline can satisfy all the 4 requirements proposed early in Section 3.4.

4 Controller Design

In this section, the backstepping method is introduced to reduce the order of hydraulic manipulator dynamic model, and the robust control method is proposed to cope with the negative influence by uncertain nonlinear factors and external disturbance.

STEP I

Define the tracking error $z_1 = q(t) - q_d(t)$, and a switching-function-like quantity z_2 is defined as:

$$z_2 \triangleq \dot{z}_1 + k_1 z_1 \qquad (30)$$

where k_1 is a symmetric positive definite gain matrix.

Differential (30) and substitute into Eq. 10:

$$M_j \dot{z}_2 + C_j z_2 = u_j - \varphi_j\left(q, \dot{q}, q_{eq}, \dot{q}_{eq}\right)\theta + \Delta_j(q, \dot{q}, t) \quad (31)$$

where $\dot{q}_{eq}$ is the equivalent trajectory velocity, which can be defined as:

$$\dot{x}_2 = \dot{q} - k_1 z_1 \qquad (32)$$

The determined robust control law u_{jd} for u_j can be designed as follows:

$$u_{jd} = u_{jm} + u_{jr} + u_{js} \qquad (33)$$

$$u_{jm} = \varphi_j\left(q, \dot{q}, q_{eq}, \dot{q}_{eq}\right)\hat{\theta} \qquad (34)$$

$$u_{jr} = -k_2 z_2 \qquad (35)$$

where k_2 is a symmetric positive definite gain matrix, u_{jm} is the model compensation term to achieve better control performance, u_{jr} is the proportional feedback term designed to ensure system stability, and u_{js} is the performance robust feedback term designed to overcome the influence of nonlinear uncertainties on the manipulator. In general, θ is unknow, so $\hat{\theta}$ and $\tilde{\theta}$ is defined as the estimate and the estimation error of θ(i.e., $\tilde{\theta} = \hat{\theta} - \theta$). Substituting (33), (34) and Eqs. 35 into 31 and simplifying the resulting expression:

$$M_j \dot{z}_2 + C_j z_2 = u_{js} - k_2 z_2 + \varphi_j\left(q, \dot{q}, \dot{q}_{eq}, \ddot{q}_{eq}\right)\tilde{\theta} \\ + \Delta_j(q, \dot{q}, t) \qquad (36)$$

The performance robust feedback term ucs need to satisfy the following conditions according to the Eq. 36:

Condition I

$$z_2^T\left[u_{js} + \varphi_j\left(q, \dot{q}, \dot{q}_{eq}, \ddot{q}_{eq}\right)\tilde{\theta} + \Delta_j(q, \dot{q}, t)\right] \le \zeta_2 \quad (37)$$

where ζ_2 is a designed parameter which can be intestinal.

Condition II

$$z_2^T u_{js} \le 0 \qquad (38)$$

STEP II

According to Eq. 12, the following results can be obtained as:

$$u_{jd} = J_j^T P_{Ld} \qquad (39)$$

where $P_L = P_i A_i - P_o A_o$ represents equivalent thrust of hydraulic cylinder.

Define the pressure input error $z_3 = P_L - P_{Ld}$, the differential expression of z_p can be obtained by combining (16) (17) and Eq. 39:

$$\dot{z}_3 = \beta_e\left[-\left(V_i^{-1}A_i^2 + V_o^{-1}A_o^2\right)J_j\dot{q} + u_Q + \Delta_Q(q, \dot{q}, t)\right] \\ -\frac{dP_{Ld}}{dt} \qquad (40)$$

where $u_Q = V_i^{-1}A_i Q_i + V_o^{-1}A_o Q_o$ is the equivalent flow input of hydraulic cylinder, and also the final adjustable control input. $\frac{dP_{Ld}}{dt}$ is the total differential of the control input P_{Ld} obtained in stepI to time t, which can be divided into two part: $\frac{dP_{Ld}}{dt} = \hat{P}_{Ld} + \tilde{P}_{Ld}$. $\hat{P}_{Ld}$ is the calculable part of $\frac{dP_{Ld}}{dt}$ and $\tilde{P}_{Ld}$ is the incalculable part of $\frac{dP_{Ld}}{dt}$, which is worthy to highlight that the $\hat{P}_{Ld}$ includes the third order derivative of q_d, as mentioned in Section 3.4.

According to the results, the final adaptive robust control law based on state estimation u for u_Q can be written as follows:

$$u_{Qd} = u_{Qm} + u_{Qr} + u_{Qs} \qquad (41)$$

$$u_{Qm} = \left(V_i^{-1}A_i^2 + V_o^{-1}A_o^2\right)J_j\dot{q} + \beta_e^{-1}\hat{P}_{Ld} \qquad (42)$$

$$u_{Qr} = -k_3 z_3 \qquad (43)$$

where k_3 is a symmetric positive definite gain matrix, u_{Qm} is the model compensation term to achieve better control performance, u_{Qr} is the proportional feedback term designed to ensure system stability, and u_{Qs} is the performance robust feedback term designed to overcome the influence of nonlinear uncertainties on the manipulator.

The adjustable model compensation term u_{Qa} also can be rewritten as follow according to Property III:

$$u_{Qa} = \varphi_Q\left(q, \dot{q}, \dot{q}_{eq}, \ddot{q}_{eq}\right)\hat{\theta} \qquad (44)$$

where $\hat{\theta}$ is the parameter estimate obtained after online parameter adaptive projection.

Substituting (41),(42),(43) into Eq. 44 and simplifying the resulting expression:

$$\dot{z}_3 = \beta_e\left(u_{Qs} - k_3 z_3 + \varphi_Q\left(q, \dot{q}, \dot{q}_{eq}, \ddot{q}_{eq}\right)\tilde{\theta} \\ + \Delta_Q(q, \dot{q}, t)\right) - \tilde{P}_{Ld} \qquad (45)$$

Similar to u_{cs}, the performance robust feedback term u_{Qs} need to satisfy the following conditions according to the Eq. 45:

Condition III

$$z_3^T\left\{\beta_e\left[J_j^T z_2 + u_{Qs} + \varphi_Q\left(q, \dot{q}, \dot{q}_{eq}, \ddot{q}_{eq}\right)\tilde{\theta} \\ + \Delta_Q(q, \dot{q}, t)\right] - \tilde{P}_{Ld}\right\} \le \zeta_3 \qquad (46)$$

where ζ_3 is a designed parameter which can be intestinal.

Condition IV

$$z_3{}^T u_{Qs} \leq 0 \tag{47}$$

Theorem 1 *The tracking error z_1 and control input error z_2 and z_3 are both bounded.*

Theorem 2 *If after finite time, disturbance error, $\Delta = 0$, gets zero and the dynamic model parameters are accurate ($\tilde{\theta} = 0$), the asymptotic output tracking (or zero final tracking error) can be achieved, i.e., $z_1 \to 0$ as $t \to 0$.*

The proof for theorem is given in Appendix.

Remark 1 Theorem I shows that the proposed controller possesses the exponentially converging transient performance, and the exponential convergence rate and final tracking error can be adjusted by some controller parameters.

Remark 2 Theorem II shows that the multi joint hydraulic manipulator system can achieve the great control performance in the presence of accurate model parameters.

Remark 3 Since u_Q is the function of Q_i and Q_o, x_v can be inversely calculated through the dynamic equation mentioned in previous section, and the actual control analog voltage U_c can be finally determined according to Eq. 20.

5 Experiment

After completing the design and implementation of visual servoing system and joint controller, in order to testing the effectiveness and reliability of the designed method, the visual servo control experiment is carried out. In the experiment, the desired joint trajectory generated by the visual servo system will be used as the input of the joint controller, so as to realize the function of target tracking. Specifically speaking, the ultimate goal of the experiment is to drive the manipulator gripper following the moving object stably with the aid of visual servo.

5.1 Experimental Setup

In order to verify the effectiveness of the visual servo control system, the experiment will be conducted on a 5-DOF hydraulic manipulator visual experiment platform, and the platform is shown in Fig. 7. The 5-DOF hydraulic manipulator consists of five parts: elbow, big arm, small arm, wrist and gripper. The platform has necessary attachments for motion control experiments, such as joint angle sensors, high-performance servo valve, high precision pressure sensors, etc. These sensors and hydraulic servo valve use
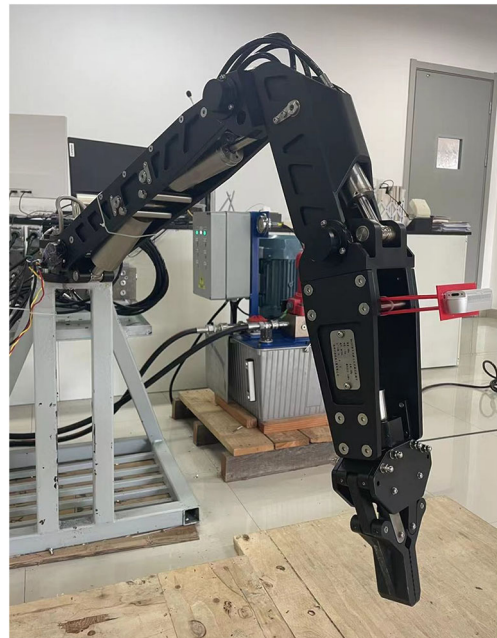

Fig. 7 Experimental Platform

Quanser high precision signal acquisition card to complete signal acquisition and output.

In addition to hydraulic manipulator, depth camera and upper computer are also used in experiment. The depth camera is mounted as eye-in-hand configuration, which is fixed near the end-effector (gripper) of the manipulator to obtain the color image and depth image of the scene in front of the end-effector. Then the color and depth images collected by the depth camera will be transmitted to the upper computer for processing, and the desired joint trajectory generated according to the target object information extracted from the color and depth image will be used as the input of the determined robust controller, which will control the multi-joint hydraulic manipulator to approach the target.

For the accuracy of kinematics calculation and solution, it is necessary to measure and calibrate the experimental object's structural parameters. Table 1 shows the main structural parameters of the Multi-DOF hydraulic manipulator (represented by D-H parameters for the convenience of kinematic modeling in Section 2.1), including the rotation range of each joint and the length information of the connecting rod.

In terms of software, Microsoft Visual Studio development tools and OpenCV 3.4.2 library are used to complete the C++ program development of depth camera image information processing. The determined robust controller was implemented using Mathworks MATLAB and Simulink software platform, and the Simulink model program was implemented using Quarc toolkit for experiments.

Table 1 D-H parameters of Multi-DOF Hydraulic Manipulator

	Joint Angle $q(°)$	Torsion Angle $\alpha(°)$	Link Length $l(mm)$	Deviation $d(mm)$
Elbow (Joint 1)	$q_1 \in [-60, 60]$	90	90	0
Big Arm (Joint 2)	$q_2 \in [-82, 38]$	0	605	0
Small Arm (Joint 3)	$q_3 \in [42, 152]$	0	290	0
Wrist (Joint 4)	$q_4 \in [-30, 72]$	0	477	0

5.2 Experimental Result

At the beginning of the experiment, the long rod affixed with ArUco code reaches into the field of the depth cameras vision, and the visual servo control system is turned on, so that the hydraulic manipulator gripper together with the camera move to the position of 50cm height above the target along the planned trajectory, which ensures the depth camera being always oriented towards the target during the movement.

In the part of visual target recognition and trajectory planning, the PBVS system speed is 20Hz mainly due to the limit of ArUco recognition and image displaying speed (the following data processing steps take little time). According to the target position recognized, the velocity-limited interpolation method proposed in this paper interpolates the actual trajectory in real time to ensure that the velocity of the operation trajectory requiring inverse

kinematics conversion is bounded (as in the enlarged figure in Fig. 8, the velocity constraint can be carried out through the interpolation algorithm when the target motion velocity changes too large).

And as can be seen from Fig. 8, the movement of the target object and the movement of the hydraulic manipulator can be roughly divided into two stages during the whole experiment. The first stage is the following stage, that is, the hand-held target moves around and the manipulator follows it in real time. The second stage is the stabilizing stage, at which the target object is placed back to the original position, and the manipulator is stabilized above the target object. The following stage span is around 0-90s, and the stable stage span is around 90-120s. And it can be seen that during the experiment, the motion range of the target object has reached 35cm, 38cm and 46cm respectively on X, Y and Z axes, which traverses most of the working space of the manipulator, so as to test and verify the control effect of

Fig. 8 Velocity-limited Interpolation Result
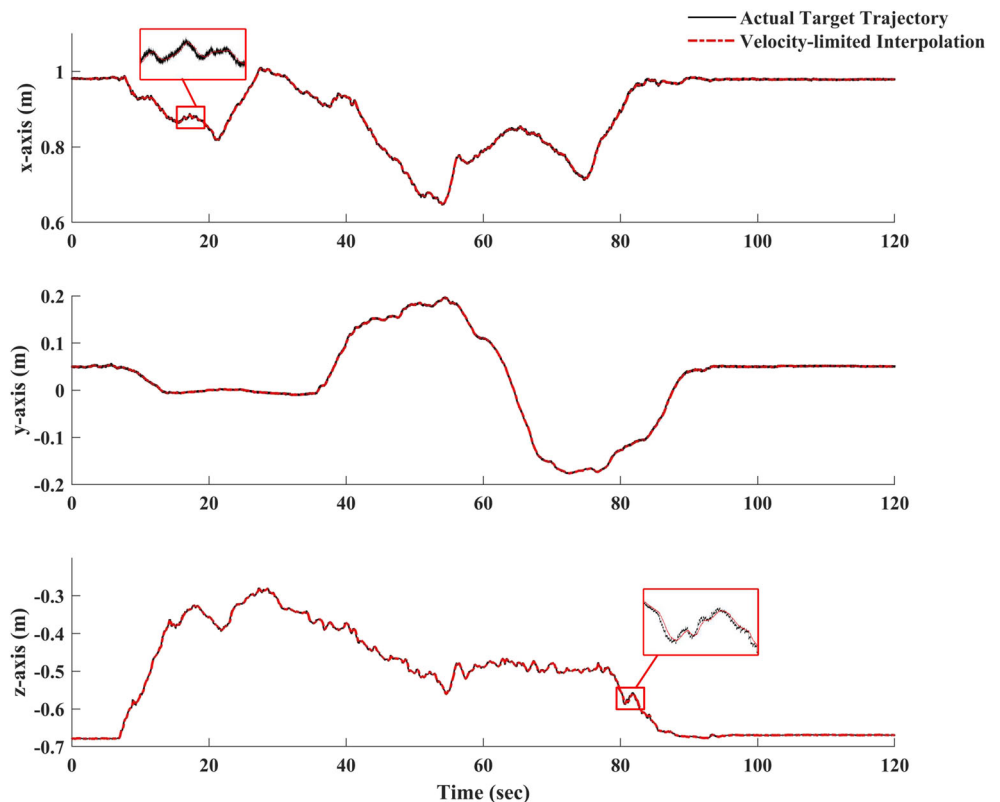
the visual servo control system of the manipulator in various positions. It should be noted that in the velocity-limited interpolation process, the error depends on the velocity of the actual trajectory. Because the interpolation result is based on the limited velocity, when the actual trajectory velocity reaches too high, the interpolator will smoothen it to ensure the operation safety of the manipulator in the process of experiment. Taking the enlarged parts in Fig. 8 as an example, the fluctuation in X-axis reaches 0.0201mand the peak velocity when fluctuating is about 0.0123m/s, while the fluctuation in Z-axis is about 0.0282m and the peak velocity when fluctuating is about 0.0243m/s, that is, the peak velocity in Z-axis when fluctuating is almost twice as in X-axis. So the interpolation error of Z-axis seems to be greater than that of X- and Y-axis.

Then, according to the results of velocity-limited interpolation, the inverse kinematics transformation can be carried out to obtain the corresponding angle value in the joint space. Then, the trajectory planning of the interpolation point is carried out through the B-spline trajectory planner to ensure that the planned trajectory that will be used as

the reference trajectory of the joint controller is smooth and third-order derivable. The results of trajectory planning are shown in the Fig. 9.

As can be seen from Fig. 9, the planned angle trajectory processed by B-spline-based planner is smooth, continuous and third-order differentiable. The trajectory avoids the problems of not smoothened motion trajectory and discontinuous motion velocity caused by manual operation during experiment, so as to meet the requirements for the ideal trajectory which has been highlighted in previous controller design section.

The comparison between the desired trajectory generated by B-spline curve trajectory planner and the measured actual trajectory of joint angle is shown in Fig. 10.

It can be seen that the angle control error of each joint is within 10° in following stage. The large error is mainly caused by the shaking of the hand-held rod followed target equipped. In the stable stage, the angle control errors of the four joints are all within 1°, and there is almost no steady-state error. As the position and pose of the target object and hydraulic manipulator change constantly, the
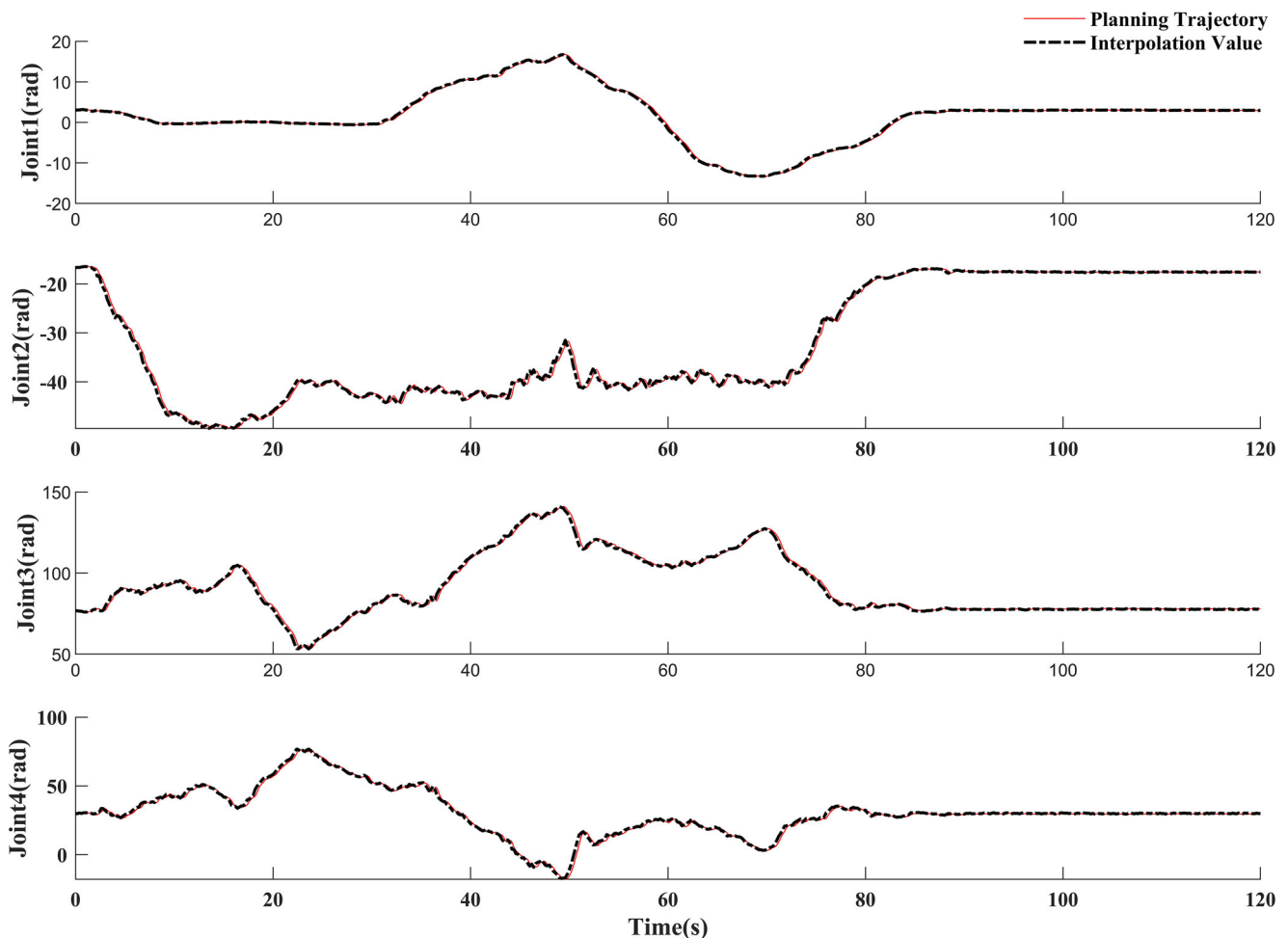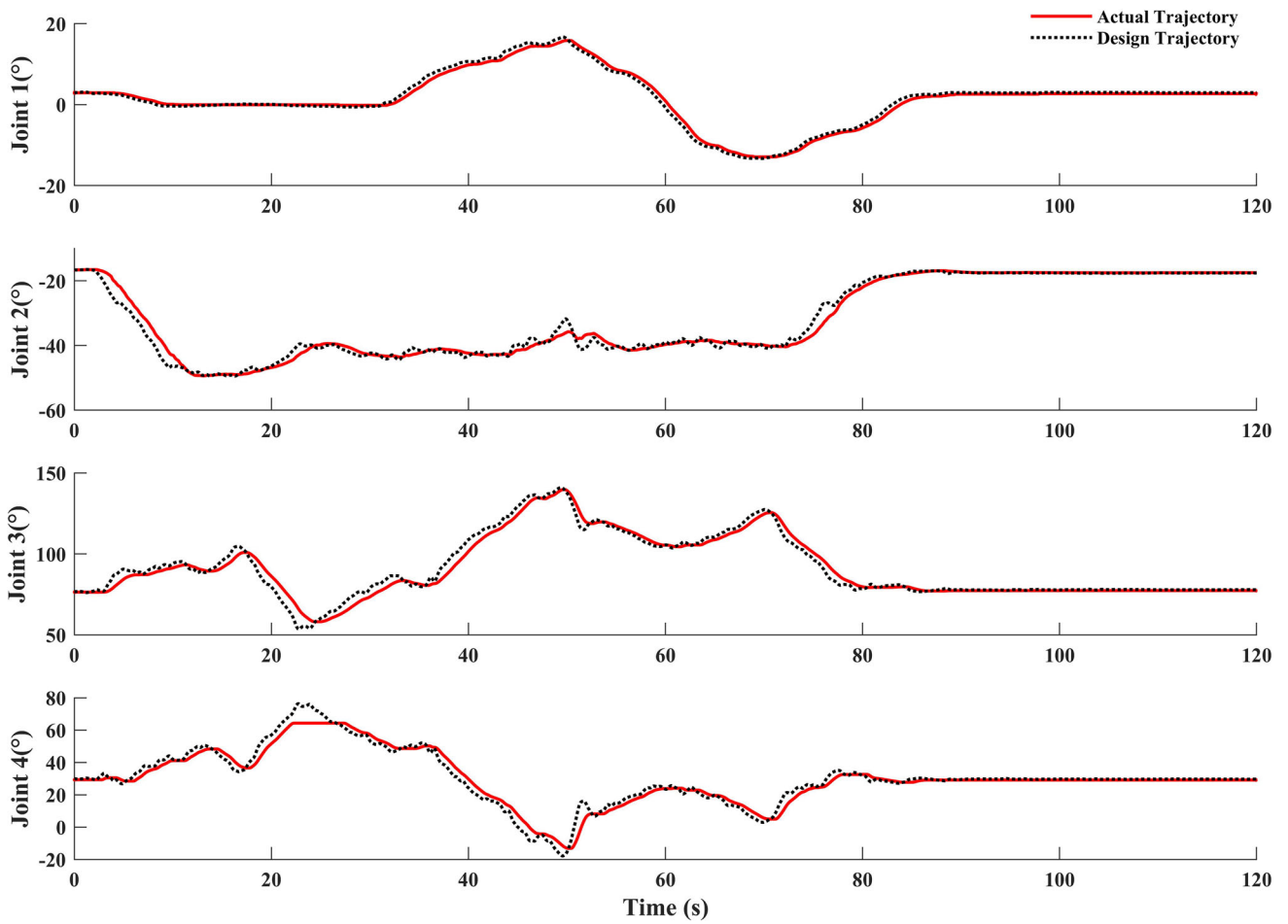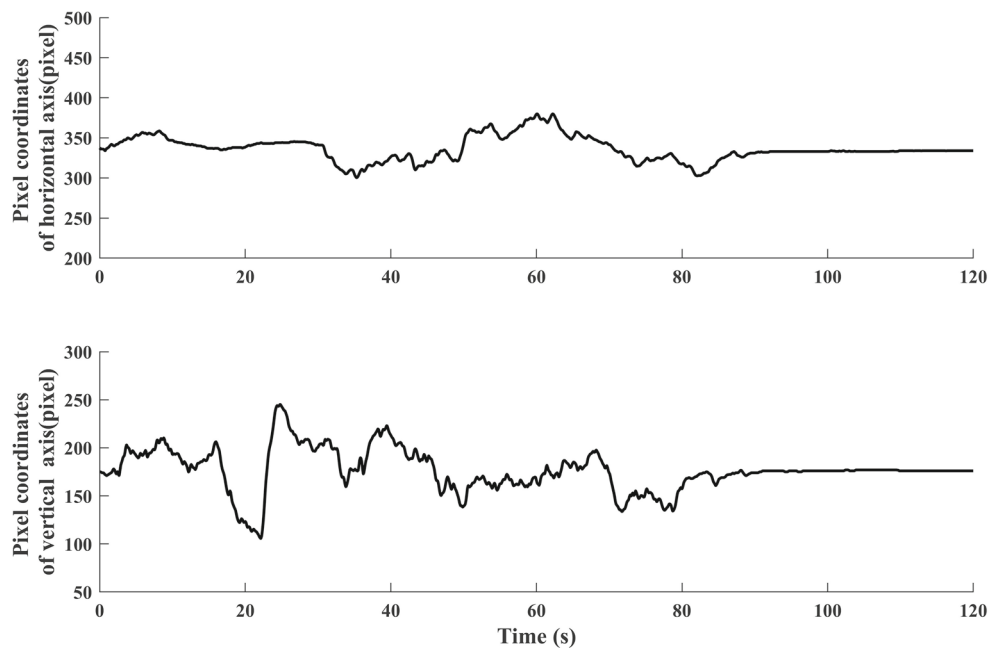

Fig. 9 Trajectory Planning Result

Fig. 10 Tacking Result of Manipulator Joints

Fig. 11 The change curve of pixel coordinates in the center of the target object

position of the relative depth camera of the target object also changes constantly. During the whole experiment, the pixel coordinate track of the target object center in the depth camera image is shown in Fig. 11. According to pixel coordinates, camera parameters and depth information of the target object, the position coordinate changes of the target object relative to the camera can be obtained, as shown in Fig. 12.

It can be seen from the Fig. 11 that the targets final position in pixel space is not exactly the center in the image, which means the steady-state error exists in position control. It is because the optical axis of camera lens is not parallel with the orientation vector of the gripper, and the color image cannot be perfectly aligned with the depth image, consequently a variety of factors cause error of camera external parameters calibration. Similarly, the relative position of the gripper is not exactly at 0.5m directly above the target at the stabilization stage. It is also mainly due to the angle and position deviation of camera installation and the inaccurate calibration of external

parameters. Despite of the steady-state error, the remaining perturbation in control error is only about 1mm at steady-state(which can be seen in Fig. 12), which indicates the satisfactory stability performance of the visual servo system and joint controller. Even in the following stage, gripper position control error remains at centimeter level.

The control input voltage of each joint hydraulic servo-valve is illustrated in Fig. 13, in which the input voltage is always bounded in $\pm 10V$, thus the problem of input saturation does not exhibit during the experiment, indicating that the backstepping controller is always performing well to meet the motive controlling requirement without the interference of input limit.

According to the experimental results, it can be concluded that the visual servo control method designed in this paper can follow the target object autonomously and stably stay over the target object. Moreover, it exhibits millimeter-level perturbation in position control during following stage, and can guarantee centimeter-level position dynamic tracking error even when the target object has
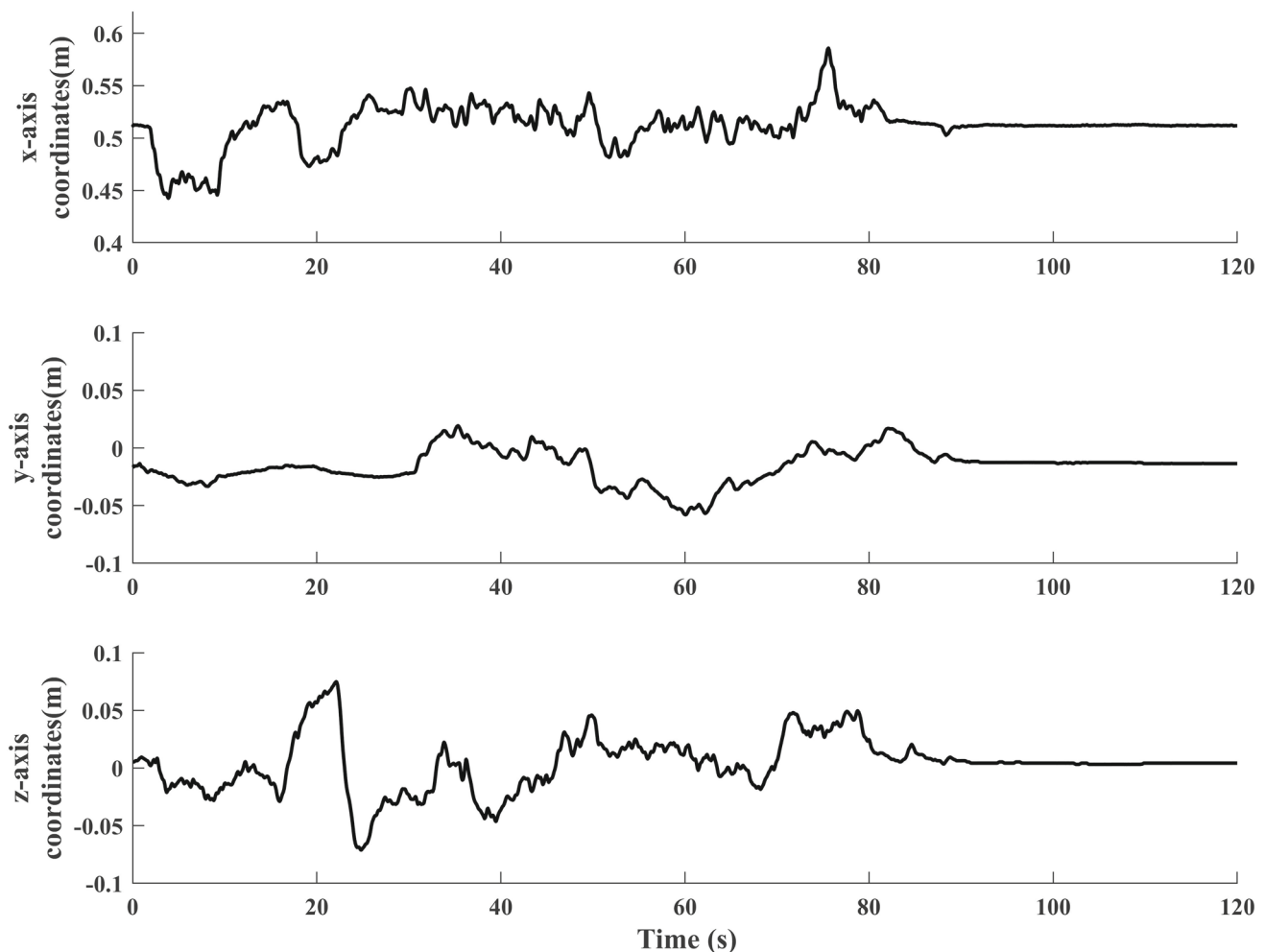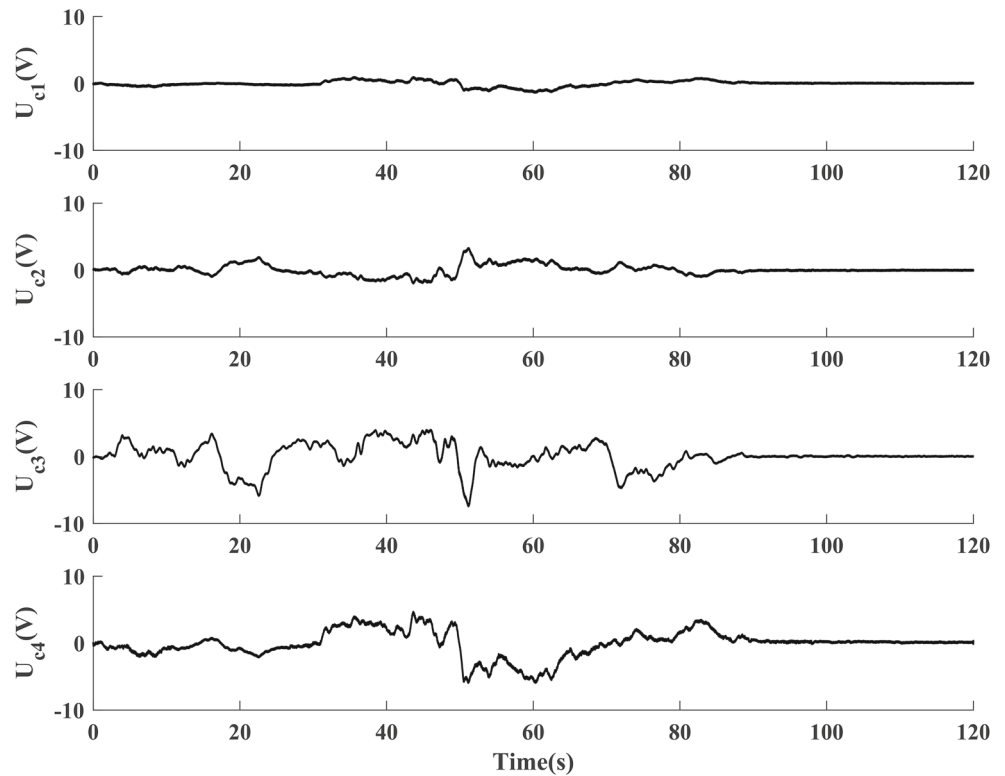

Fig. 12 The position of the object relative to the camera

Fig. 13 Control Input Result

more than 0.1m/s motion speed and several centimeters of chambering. Despite of the adverse effect caused by camera calibration error, the control error in pixel space is within 1 pixel, which can well indicate that the visual servo system has made full use of visual signals to improve the precision and stability of the position control.

5.3 Comparative Analysis

After conducting experiments, it is necessary to verify the effectiveness and robustness of the proposed position-based visual servoing method, and the comparison simulation of proposed and classical PBVS is done. Because the backstepping controller and the visual servoing method are independent parts in this paper, and the simulation results suggest that the classical interaction matrix-based PBVS is not suitable to the backstepping controller (to be demonstrated in later simulation analysis), it is the comparison simulations excluding backstepping controller that are conducted, instead of experiments.

For comparison, the interaction matrix-based PBVS is also simulated as a benchmark method, which is expressed as follows:

$$\dot{q}_d = -\lambda L^{\dagger} \mathbf{e}_p \tag{48}$$

where $\mathbf{e}_p = \mathbf{p}_{\text{gripper}} - \mathbf{p}_{\text{target}}$ is the error of gripper position, and $L = \left\| \mathbf{p}_{\text{gipper}} - \mathbf{p}_{\text{taxget}} \right\| J$ is the interaction

matrix, which represents the transformation from gripper position error to joint angular velocity $\dot{q}_d$, and λ is a constant coefficient (take 0.1 in simulation). J is the Jacobian matrix between gripper velocity and joint angular velocity, and $L^{\dagger} = \left(L^T L\right)^{-1} L^T$ is the Moore-Penrose pseudo-inverse of L.

In simulation, two different working conditions are applied.
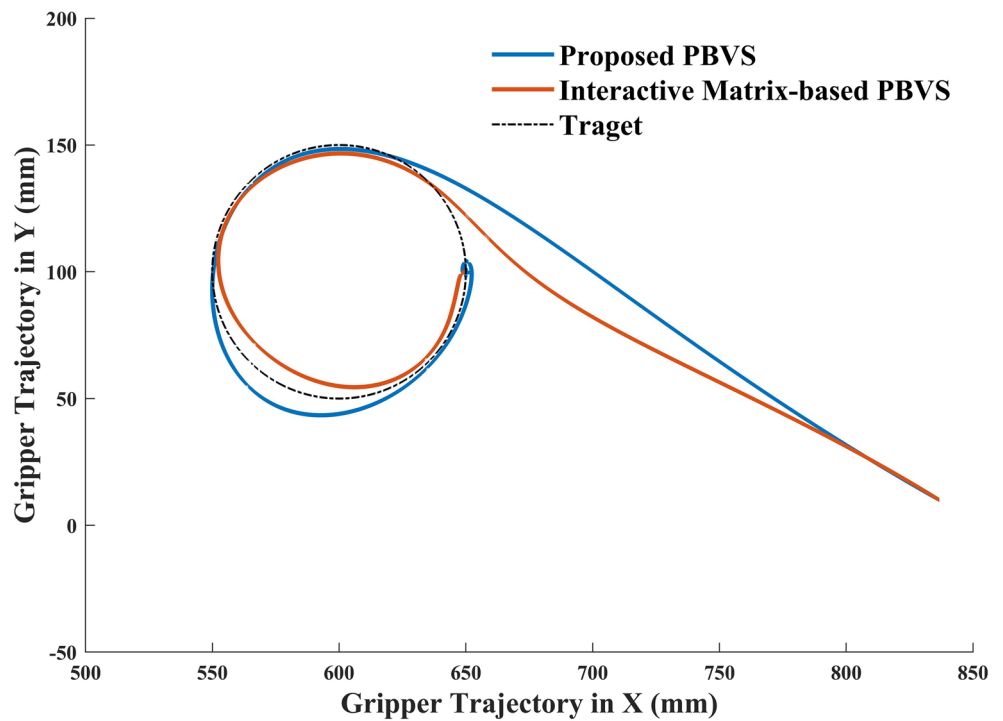
Working Condition I

Target trajectory obeys (49), turning a cycle in first 10 seconds and being steady in last 10 seconds. The calibration error of joint angles are respectively set as $-3°$, $-10°$, $17°$ and $-17°$, while the calibration error of camera position and orientation are set over 10mm and $10°$(which are quite huge calibration errors and almost impossible in experiments).

$$\mathbf{p}_{\text{object}} = \begin{cases} \begin{bmatrix} 100 + 50\cos(0.2\pi t) \\ 650 + 50\sin(0.2\pi t) \\ -700 \end{bmatrix} (\text{mm}), t \leq 10 \text{ s} \\ \begin{bmatrix} 100 \\ 700 \\ -700 \end{bmatrix} (\text{mm}), 10 \text{ s} < t \leq 20 \text{ s} \end{cases} \tag{49}$$

Working Condition II

Target trajectory obeys (50), turning two cycles during 20s with object position trembling. In Eq. 50, the $n(t)$ represents the target positioning noise, which is limited in

Fig. 14 Manipulator Gripper Tracking Trajectories at Global Coordinates in Working Condition I


1mm. The calibration error of joint angles and camera pose are set as the same value as in Working Condition I.

$$\mathbf{p}_{\text{object}} = \left\{ \begin{bmatrix} 100 + 50\cos(0.2\pi t) + n(t) \\ 650 + 50\sin(0.2\pi t) + n(t) \\ -700 \end{bmatrix} \right. \text{(mm)}, t \leq 20s \quad (50)$$

In Working Condition I, both the interaction matrix-based and proposed PBVS methods are able to track moving target (in first 10s) and ensure the error converge (in last 10s). In simulation, these two methods generate the trajectories of manipulator gripper, which are shown in Fig. 14 with target trajectory.

Fig. 15 Distance between Actual Position and Desired Position of Gripper in Working Condition I
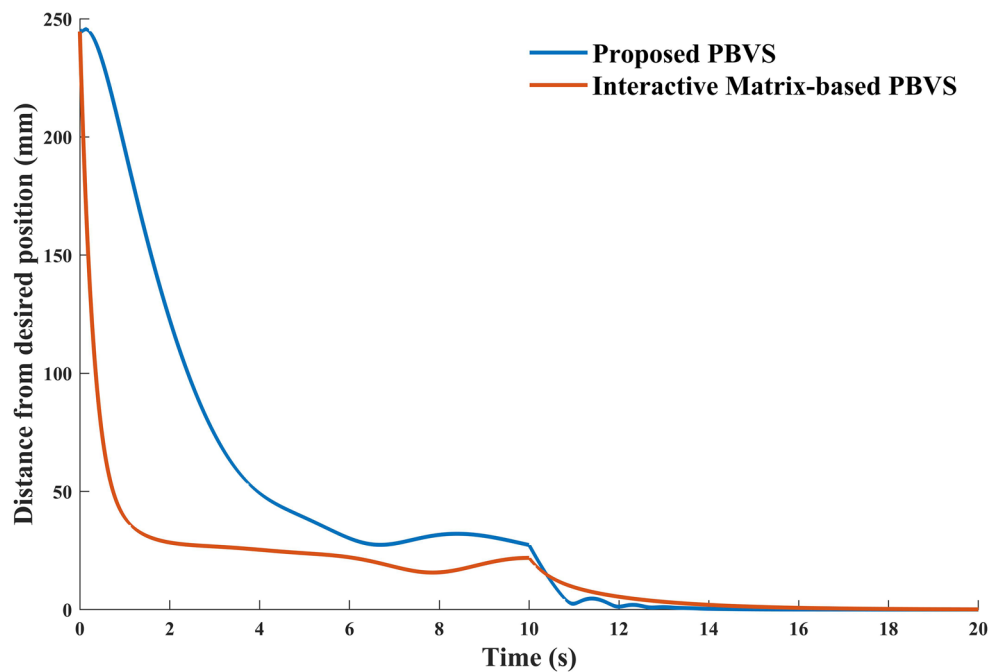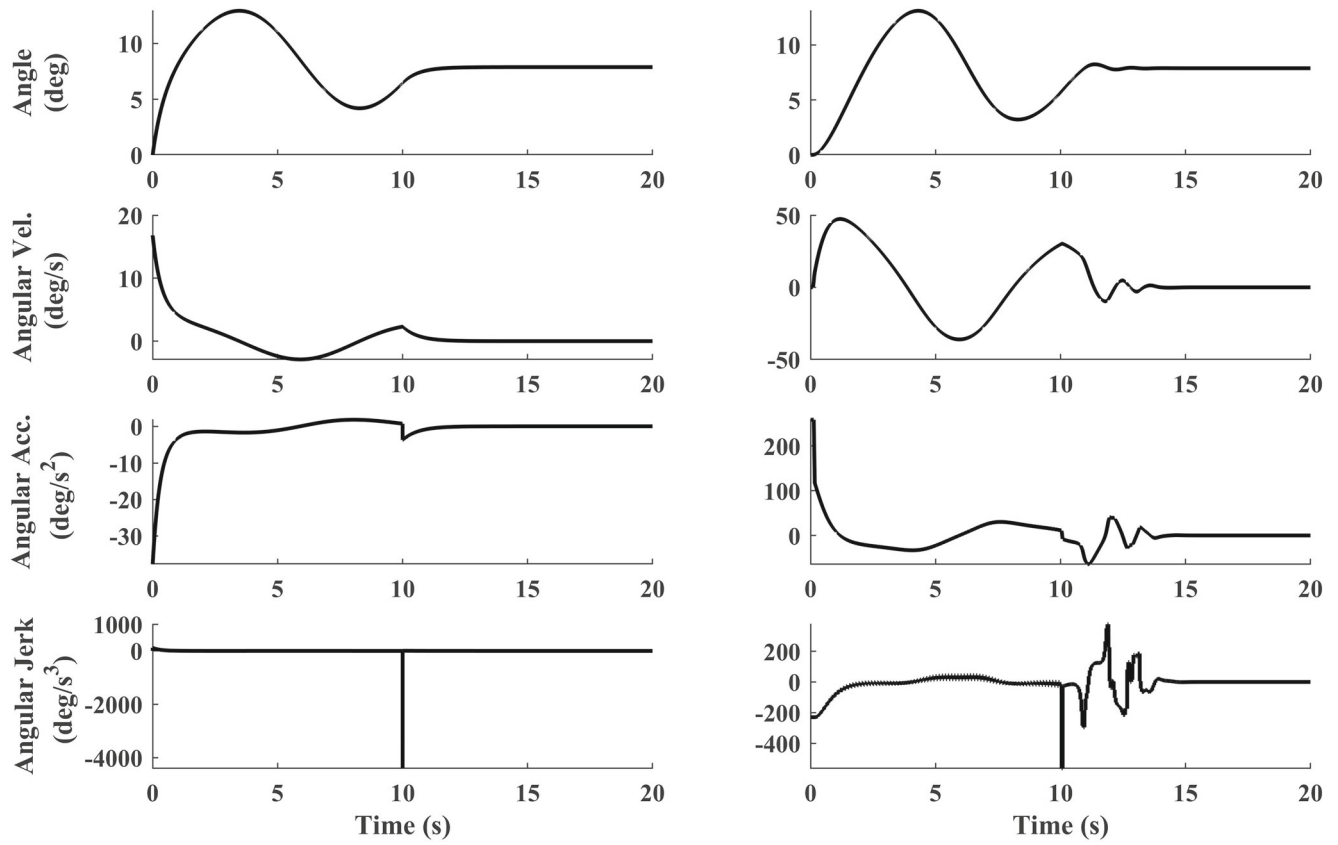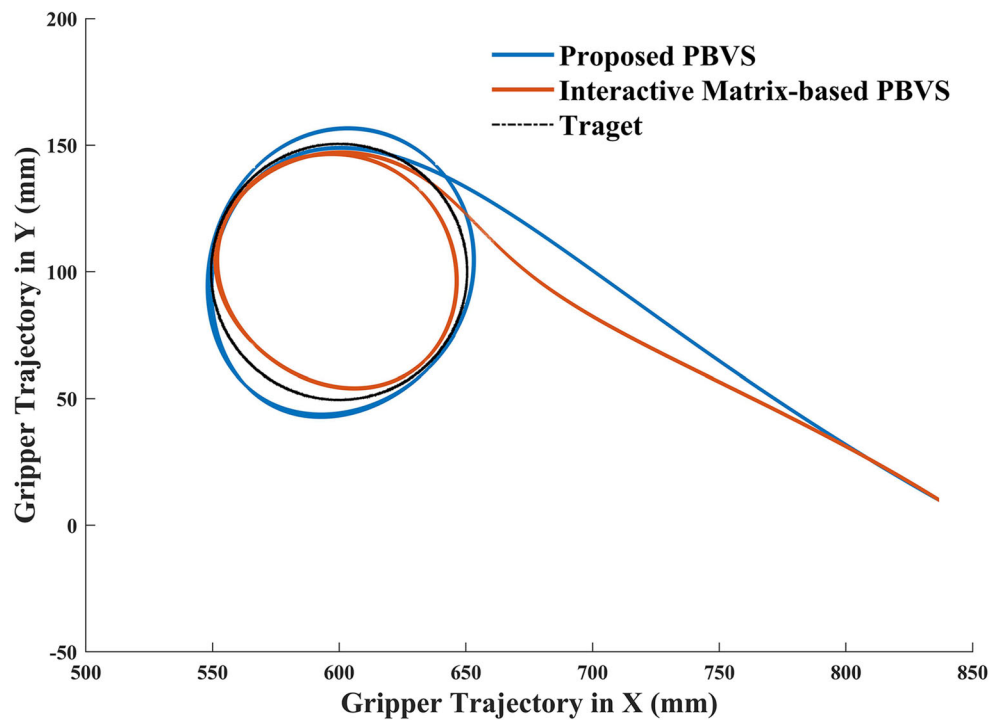
Fig. 16 Comparison Curve of Joint-1 in Working Condition I

Fig. 17 Manipulator Gripper Tracking Trajectories at Global Coordinates in Working Condition II

Taking the distance between grippers actual position and desired position as the vertical axis, then the distance-time curves during simulation are shown in Fig. 15.

It can be seen that when gripper is far from the desired position, interaction matix-based method reaches faster converge velocity, but these two methods both obtain dynamic error around 30mm. However, when the target becomes static (in last 10s), the converge velocity of proposed PBVS method is obviously faster than interaction matrix-based method.

Except from the tracking velocity and accuracy, it is the joint angle trajectory differentiability that needs to be inspected to meet the requirement of backstepping controller. Take the joint-1 as an example, the angle, angular velocity, angular acceleration and angular jerk generated by these two methods are shown in Fig. 16 for comparison.

It can be seen that at 10s (the time target becomes static), the first joint angular acceleration by interaction matrix-based method suddenly changes, which means the angular jerk will be infinite at 10s (the angular jerk approximately obtained by difference gets over $-4000°/s^3$, a really huge and unacceptable value). That is, even when target position stays continuous, the sudden change of target velocity would cause the infinity of angle third derivatives generated by interaction matrix-based method. Since there

are sudden changes of target position and velocity caused by target trembling, positioning noise and target velocity, the joint angle trajectories generated by interaction matrix-based method would be inapplicable when the manipulator is controlled by the proposed controller (the controller designed in this paper requires the existence of the third derivative of the target trajectory).

In order to verify the wide applicability of the proposed PBVS method, the simulation in Working Condition II (with continuous mutation and noise of target position) is conducted to inspect the angle third derivative boundedness. The trajectories of manipulator gripper together with target trajectory in simulation are shown in Fig. 17.

Although these two methods both track the moving target with positioning noise all the process, Fig. 18 showing the first joint angle, angular velocity, angular acceleration and angular jerk suggests the difference of these two methods. Even the target position and velocity are always continuous and the positioning noise is limited within 1mm, the angular jerk generated by interaction matrix-based method reaches over $200000°/s^3$, which is actually fatal to the proposed backstepping controller (taking angular jerk as input) in experiment. At the same time, the angular jerk stays within $\pm500°/s^3$ when the proposed PBVS method is applied, which is quite more acceptable.
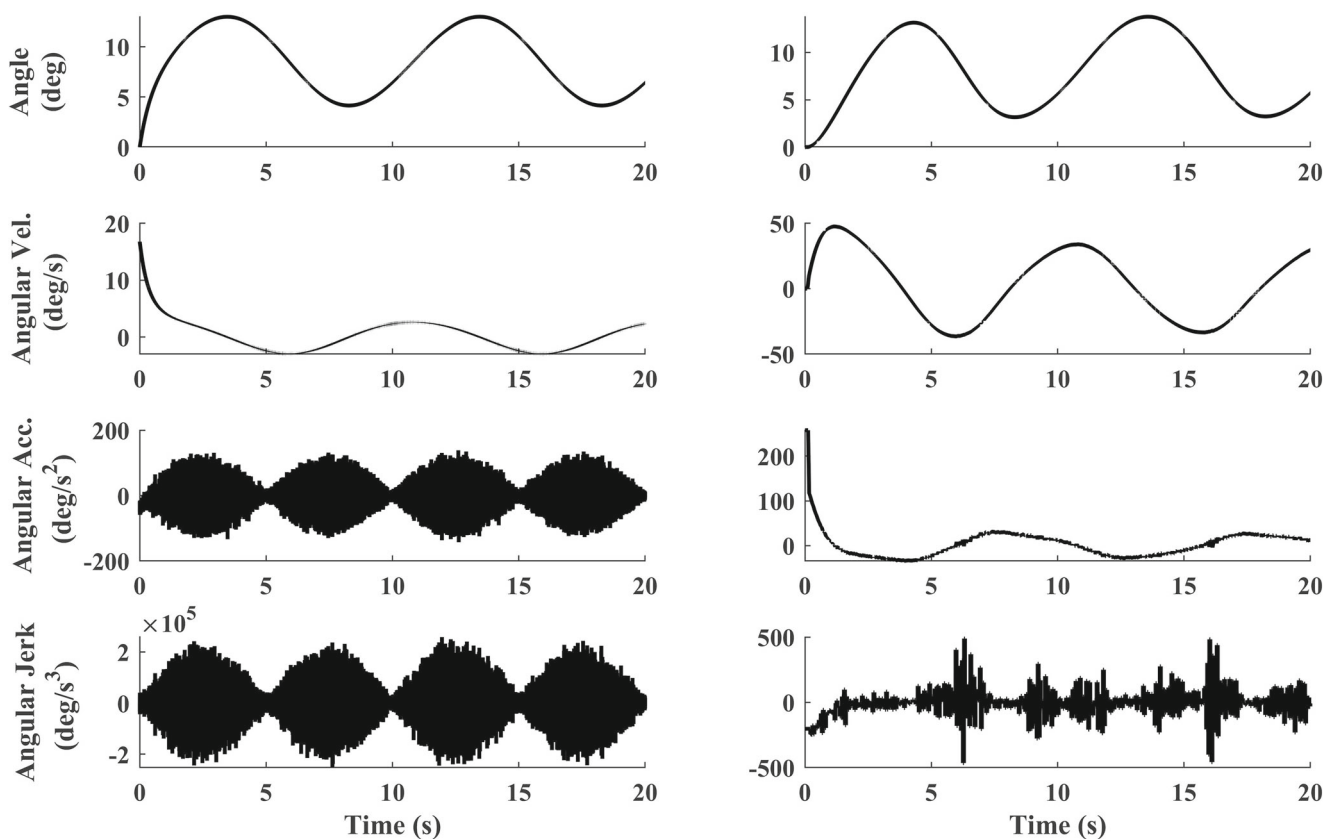

Fig. 18 Distance between Actual Position and Desired Position of Gripper in Working Condition II

6 Conclusion

In this paper, a position based visual servoing control method is proposed to realize the function of autonomous target object following for hydraulic manipulator. The visual servoing system is configured by eye-in-hand style with the basis of a depth camera. In term of the algorithm, in addition to the conventional PBVS method, a velocity-limited path interpolation is proposed to generate discrete path points in 3D space with the adjustable velocity limit, then the inverse kinematics is improved to be well-constrained to cope with the nonstandard DoF number of the hydraulic manipulator platform, and a trajectory planner based on 4-dimensional cubic B-spline is designed to generate third order differentiable desired trajectory for joint angles, which meets the trajectory differentiability requirement. A backstepping controller is proposed to achieve good robustness to overcome unmeasurable disturbance and ensure the stable performance during movement. To verify the effectiveness of the position based visual servoing control system, an experiment is conducted on the platform mainly consisting of a 5-DoF hydraulic manipulator and an RGB-D camera, and it is shown to follow the moving target successfully, thus the feasibility and reliability is well reflected. In the future work, more specific visual object recognition method of hydraulic manipulator will be develop and more complex operation tasks of hydraulic manipulator will be conducted to improve the applicability of the designed visual servo control method.

Appendix A: Proof for Theorem

Proof for Theorem I The Lyapunov function is defined as:

$$V_2 = \frac{1}{2} z_2^T M_j z_2 \tag{A1}$$

$$V_3 = V_2 + \frac{1}{2} z_3^T z_3 \tag{A2}$$

Combine (31),(33), (34), (35) and Eq. A1 the differential of V_2 can be simplified as:

$$\dot{V}_2 = J_j^T z_2 z_3 - z_2^T k_2 z_2 + z_2^T$$
$$\left[J_j u_{js} - \varphi_c \left(q, \dot{q}, \dot{q}_{eq}, \ddot{q}_{eq} \right) \tilde{\theta} + \Delta \left(q, \dot{q}, t \right) \right] \tag{A3}$$

Combine (41), (42), (43) and (A2), the differential of V_3 can be simplified as:

$$\dot{V}_3 = \dot{V}_3|_{z_3=0} + z_3^T \left[J_j^T z_2 + \beta_e \left[u_{Qs} - k_3 z_3 \right. \right.$$
$$\left. \left. + \varphi_Q \left(q, \dot{q}, \dot{q}_{eq}, \ddot{q}_{eq} \right) \tilde{\theta} + \Delta_Q \left(q, \dot{q}, t \right) \right] - \tilde{P}_{Ld} \right] \tag{A4}$$

According to the Condition III, (A4) can be convert to inequality form as follow:

$$\dot{V}_3 \leq \dot{V}_2|_{z_3=0} - k_3 z_3 + \zeta_3 \tag{A5}$$

$\dot{V}_2|_{z_3=0}$ can be written as:

$$\dot{V}_2|_{z_3=0} = z_2^T \left[-k_2 z_2 + J_j u_{js} - \varphi_j \left(q, \dot{q}, \dot{q}_{eq}, \ddot{q}_{eq} \right) \tilde{\theta} \right.$$
$$\left. + \Delta_Q \left(q, \dot{q}, t \right) \right] \tag{A6}$$

According to the Condition I, (A6) can be convert to inequality form as follow:

$$\dot{V}_2|_{z_3=0} \leq -z_2^T k_2 z_2 + \zeta_2 \tag{A7}$$
$$\leq -\eta_2 V_2 + \zeta_2 \tag{A8}$$

where $\eta_2 = 2 M_j^{-1} k_2$, the following equation can be obtained by solving (A8) in time domain:

$$V_2|_{z_3=0}(t) \leq V_2|_{z_3=0}(0) e^{-\eta_2 t} + \frac{\zeta_2}{\eta_2} \left(1 - e^{-\eta_2 t} \right) \tag{A9}$$

According to Eq. A9, $V_2|_{z_3=0} \leq \frac{\zeta_2}{\eta_2}$, and $V_2|_{z_3=0} \to 0$ as $t \to \infty$.

Combined (A6) and Eq. A9, the following inequality of $\dot{V}_3$ can be obtained the as:

$$V_3 \leq -\eta_3 V_3 + \zeta_3 + \frac{\eta_3}{\eta_2} \zeta_2 \tag{A10}$$

where $\eta_3 = 2 k_3$, the following equation can be obtained by solving (A8) in time domain:

$$V_3(t) \leq V_3(0) e^{-\eta_3 t} + \frac{\zeta_c}{\eta_c} \left(1 - e^{-\eta_3 t} \right) \tag{A11}$$

where $\frac{\zeta_c}{\eta_c} = \frac{\zeta_2}{\eta_2} + \frac{\zeta_3}{\eta_3}$.

According to Eq. A11, $V_3 \leq \frac{\zeta_c}{\eta_c}$, and $V_3 \to 0$ as $t \to \infty$.

It can be proved that V3 is ultimately bounded to $\frac{\zeta_c}{\eta_c}$ and z_3 is bounded. On the premise that z_3 is bounded, according to eq.49, V_2 is ultimately bounded to $\frac{\zeta_2}{\eta_2}$ and z_2 is bounded.

In addition, by frequency domain transformation of Eq. 30, the conversion function $L(s)$ between z_1 and z_2 can be obtained as follows:

$$L(s) = \frac{z_1}{z_2} = \frac{1}{s + k_1} \tag{A12}$$

According to Eq. 30, z_1 is bounded on the premise that z_2 is bounded. The proof for Theorem I is complete. □

Proof for Theorem II When disturbance error, $\Delta = 0$, gets zero and the dynamic model parameters are accurate ($\tilde{\theta} = 0$), the differential of Lyapunov function such as Eqs. A2 and A4 can be rewritten as:

$$\dot{V}_2 = J_j^T z_2 z_3 - z_2^T k_2 z_2 + z_2^T J_j u_{js} \tag{13}$$

$$\dot{V}_3 = \dot{V}_3|_{z_3=0} + z_3^T \left[J_j^T z_2 + \beta_e \left[u_{Qs} - k_3 z_3 \right] - \tilde{P}_{Ld} \right] \tag{14}$$

According to Condition II, the upper bound of Eq. 13 can be expressed as:

$$\dot{V}_2|_{z_3=0} \leq -z_2^T k_2 z_2 \leq 0 \tag{15}$$

According to Condition IV, (14) can be rewritten as:

$$V_3 \leq -z_3{}^T k_3 z_3 \leq 0 \tag{16}$$

Thus, the asymptotic output tracking of Step II in the process of control law design is achieved, i.e., $z_3 \to 0$ as $t \to \infty$. And on this premise, the asymptotic output tracking of Step I is also achieved.

$$\dot{V}_2 = \dot{V}_2|_{z_3=0} \leq -z_2{}^T k_2 z_2 \leq 0 \tag{17}$$

That is,

$$z_2 \to 0$$

as $t \to \infty$.

And according to Eq. 30, $z_1 \to 0$ can be achieved on the premise of that $z_2 \to 0$ as $t \to \infty$. The proof for Theorem 2 is complete. □

Declarations

Conflict of Interests The authors declare that they have no known competing financial interests or personal relationships that could have appeared to influence the work reported in this paper.

References

1. Mohammad Hossein Fallah, M., Janabi-Sharifi, F.: Conjugated visual predictive control for constrained visual servoing. J. Intell. Robot. Syst **101**(2), 33 (2021). https://doi.org/10.1007/s10846-020-01299-6
2. Mattila, J., Koivumki, J., Caldwell, D.G., Semini, C.: A survey on control of hydraulic robotic manipulators with projection to future trends. IEEE ASME Trans. Mechatron. **22**(2), 669–680 (2017). https://doi.org/10.1109/TMECH.2017.2668604
3. Kornuta, T., Zieliński, C.: Robot control system design exemplified by multi-camera visual servoing. J. Intell. Robot. Syst **77**(3), 499–523 (2015). https://doi.org/10.1007/s10846-013-9883-x
4. Sadeghzadeh, M., Calvert, D., Abdullah, H.A.: Self-learning visual servoing of robot manipulator using explanation-based fuzzy neural networks and q-learning. J. Intell. Robot. Syst **78**(1), 83–104 (2015). https://doi.org/10.1007/s10846-014-0151-5
5. Shen, W., Wang, J.: An integral terminal sliding mode control scheme for speed control system using a double-variable hydraulic transformer. ISA Transactions. https://doi.org/10.1016/j.isatra.2019.08.068 (2019)
6. Li, H., Zhang, X.m., Zeng, L., Huang, Y.j.: A monocular vision system for online pose measurement of a 3rrr planar parallel manipulator. J. Intell. Robot. Syst **92**(1), 3–17 (2018). https://doi.org/10.1007/s10846-017-0720-5
7. Yao, J., Deng, W.: Active disturbance rejection adaptive control of hydraulic servo systems. IEEE Trans. Ind. Electron. **64**(10), 8023–8032 (2017). https://doi.org/10.1109/TIE.2017.2694382
8. Daniilidis, K., Bayro-Corrochano, E.: The dual quaternion approach to hand-eye calibration. In: Proceedings of 13th International Conference on Pattern Recognition, vol. 1, pp. 318–3221 (1996). https://doi.org/10.1109/ICPR.1996.546041
9. Ali, Z.A., Israr, A., Alkhammash, E.H., Hadjouni, M.: A leader-follower formation control of multi-uavs via an adaptive hybrid controller. Complexity 2021. https://doi.org/10.1155/2021/9231636 (2021)
10. Elsisi, M., Mahmoud, K., Lehtonen, M., Darwish, M.M.: An improved neural network algorithm to efficiently track various trajectories of robot manipulator arms. Ieee Access **9**, 11911–11920 (2021). https://doi.org/10.1109/ACCESS.2021.3051807
11. Ali, Z.A., Xinde, L.: Modeling and controlling the dynamic behavior of an aerial manipulator. Fluctuation and Noise Letters, 2150044. https://doi.org/10.1142/S0219477521500449 (2021)
12. Bodie, K., Tognon, M., Siegwart, R.: Dynamic end effector tracking with an omnidirectional parallel aerial manipulator. IEEE Robot. Autom. Lett **6**(4), 8165–8172 (2021). https://doi.org/10.1109/LRA.2021.3101864
13. Thelen, A., Frey, S., Hirsch, S., Hering, P.: Improvements in shape-from-focus for holographic reconstructions with regard to focus operators, neighborhood-size, and height value interpolation. IEEE Trans. Image Process. **18**(1), 151–157 (2009). https://doi.org/10.1109/TIP.2008.2007049
14. Yao, J., Deng, W., Jiao, Z.: Rise-based adaptive control of hydraulic systems with asymptotic tracking. IEEE Trans. Autom. Sci. Eng. **14**(3), 1524–1531 (2017). https://doi.org/10.1109/TASE.2015.2434393
15. Sun, X., Zhu, X., Wang, P., Chen, H.: A review of robot control with visual servoing. In: 2018 IEEE 8th Annual International Conference on CYBER Technology in Automation, Control, and Intelligent Systems (CYBER), pp. 116–121 (2018). https://doi.org/10.1109/CYBER.2018.8688060
16. Keshmiri, M., Xie, W.F.: Visual servoing of a robotic manipulator using an optimized trajectory planning technique. In: 2014 IEEE 27th Canadian Conference on Electrical and Computer Engineering (CCECE), pp.1–6 (2014). https://doi.org/10.1109/CCECE.2014.6901078
17. Ren, Y., Sun, H., Tang, Y., Wang, S.: Vision based object grasping of robotic manipulator. In: 2018 24th International Conference on Automation and Computing (ICAC), pp. 1–5 (2018). https://doi.org/10.23919/IConAC.2018.8749001
18. Pan, W., Lyu, M., Hwang, K.S., Ju, M.Y., Shi, H.: A neuro-fuzzy visual servoing controller for an articulated manipulator. IEEE

Access **6**, 3346–3357 (2018). https://doi.org/10.1109/ACCESS.2017.2787738

19. Lin, C.Y., Hsieh, P.J., Chang, F.A.: Dsp based uncalibrated visual servoing for a 3-dof robot manipulator. In: 2016 IEEE International Conference on Industrial Technology (ICIT), pp. 1618–1621 (2016). https://doi.org/10.1109/ICIT.2016.7475003

20. Zhan, G., Du, D., Wang, H.: Experimental analysis of networked visual servoing inverted pendulum system under noise attacks. In: 2018 IEEE 27th International Symposium on Industrial Electronics (ISIE), pp. 971–975 (2018). https://doi.org/10.1109/ISIE.2018.8433805

21. Li, J., Huang, H., Xu, Y., Wu, H., Wan, L.: Uncalibrated visual servoing for underwater vehicle manipulator systems with an eye in hand configuration camera. Sensors 19(24) (2019). https://doi.org/10.3390/s19245469

22. Bae, S.H., Kim, E.J., Yang, S.J., Park, J.K., Kuc, T.Y.: A dynamic visual servoing of robot manipulator with eye-in-hand camera. In: 2018 International Conference on Electronics, Information, and Communication (ICEIC), pp. 1–4 (2018). https://doi.org/10.23919/ELINFOCOM.2018.8330640

23. Burger, W., Dean-Leon, E., Cheng, G.: Robust second order sliding mode control for 6d position based visual servoing with a redundant mobile manipulator. In: 2015 IEEE-RAS 15th International Conference on Humanoid Robots (Humanoids), pp. 1127–1132 (2015). https://doi.org/10.1109/HUMANOIDS.2015.7363494

24. Hwang, K.S., Lee, J.L., Hwang, Y.L., Jiang, W.C.: Image base visual servoing base on reinforcement learning for robot arms. In: 2017 56th Annual Conference of the Society of Instrument and Control Engineers of Japan (SICE), pp. 566–569 (2017). https://doi.org/10.23919/SICE.2017.8105453

25. Zhang, Y., Li, S., Liao, B., Jin, L., Zheng, L.: A recurrent neural network approach for visual servoing of manipulators. In: 2017 IEEE International Conference on Information and Automation (ICIA), pp. 614–619 (2017). https://doi.org/10.1109/ICInfA.2017.8078981

26. Wang, K., Ding, N., Dai, F.: Visual servoing based pickup of stationary objects with a dynamically controlled manipulator. In: 2017 IEEE International Conference on Industrial Technology (ICIT), pp. 902–907 (2017). https://doi.org/10.1109/ICIT.2017.7915479

27. Helian, B., Chen, Z., Yao, B.: Precision motion control of a servomotor-pump direct-drive electrohydraulic system with a nonlinear pump flow mapping. IEEE Trans. Ind. Electron. **67**(10), 8638–8648 (2019). https://doi.org/10.1109/TIE.2019.2947803

28. Bartlett, H.L., Lawson, B.E., Goldfarb, M.: Design, control, and preliminary assessment of a multifunctional semipowered ankle prosthesis. IEEE/ASME Transactions on Mechatronics **24**(4), 1532–1540 (2019). https://doi.org/10.1109/TMECH.2019.2918685

29. Cheng, M., Zhang, J., Xu, B., Ding, R., Wei, J.: Decoupling compensation for damping improvement of the electrohydraulic control system with multiple actuators. IEEE ASME Trans. Mechatron. **23**(3), 1383–1392 (2018). https://doi.org/10.1109/TMECH.2018.2834936

30. Hyon, S., Suewaka, D., Torii, Y., Oku, N.: Design and experimental evaluation of a fast torque-controlled hydraulic humanoid robot. IEEE ASME Trans. Mechatron. **22**(2), 623–634 (2017). https://doi.org/10.1109/TMECH.2016.2628870

31. Lyu, L., Chen, Z., Yao, B.: Advanced valves and pump coordinated hydraulic control design to simultaneously achieve high accuracy and high efficiency. IEEE Transactions on Control Systems Technology, pp. 1–13. https://doi.org/10.1109/TCST.2020.2974180 (2020)

32. Ding, R., Cheng, M., Jiang, L., Hu, G.: Active fault-tolerant control for electro-hydraulic systems with an independent metering valve against valve faults. IEEE Trans. Ind. Electron. **68**(8), 7221–7232 (2021). https://doi.org/10.1109/TIE.2020.3001808

33. Tripathi, A., Dasrath, D., Sun, Z., Northrop, W., Kittelson, D., Stelson, K.A.: Design and control of a controlled trajectory rapid compression and expansion machine. IEEE ASME Trans. Mechatron. **24**(4), 1711–1722 (2019). https://doi.org/10.1109/TMECH.2019.2917820

34. Huang, J., An, H., Yang, Y., Wu, C., Wei, Q., Ma, H.: Model predictive trajectory tracking control of electro-hydraulic actuator in legged robot with multi-scale online estimator. IEEE Access **8**, 95918–95933 (2020). https://doi.org/10.1109/ACCESS.2020.2995701

35. Lyu, L., Chen, Z., Yao, B.: Development of pump and valves combined hydraulic system for both high tracking precision and high energy efficiency. IEEE Transactions on Industrial Electronics **66**(9), 7189–7198 (2019). https://doi.org/10.1109/TIE.2018.2875666

36. Shen, W., Wang, J.: An integral terminal sliding mode control scheme for speed control system using a double-variable hydraulic transformer. ISA transactions. https://doi.org/10.1016/j.isatra.2019.08.068 (2019)

37. Chen, Z., Huang, F., Sun, W., Gu, J., Yao, B.: Rbf-neural-network-based adaptive robust control for nonlinear bilateral teleoperation manipulators with uncertainty and time delay. IEEE ASME Trans. Mechatron. **25**(2), 906–918 (2020). https://doi.org/10.1109/TMECH.2019.2962081

38. Sivcev, S., Rossi, M., Coleman, J., Dooly, G., Omerdic, E., Toal, D.: Fully automatic visual servoing control for work-class marine intervention rovs. Control Eng. Pract. **74**, 153–167 (2018). https://doi.org/10.1016/j.conengprac.2018.03.005

39. Chen, Z., Huang, F., Chen, W., Zhang, J., Sun, W., Chen, J., Gu, J., Zhu, S.: Rbfnn-based adaptive sliding mode control design for delayed nonlinear multilateral telerobotic system with cooperative manipulation. IEEE Trans. Industr. Inform. **16**(2), 1236–1247 (2020). https://doi.org/10.1109/TII.2019.2927806

40. Coquillart, S.: Computing offsets of b-spline curves. Computer-Aided Design **19**(6), 305–309 (1987). https://doi.org/10.1016/0010-4485(87)90284-3

41. Wang, M., Li, X., Xu, K., Jiang, R.: Smooth trajectory planning for manipulator of cotton harvesting machinery based on quaternion and b-spline. In: 2012 International Symposium on Instrumentation Measurement, Sensor Network and Automation (IMSNA), vol. 1, pp. 134–137 (2012). https://doi.org/10.1109/MSNA.2012.6324531

42. Liang, F., Yan, G., Fang, F.: Global time-optimal b-spline feedrate scheduling for a two-turret multi-axis nc machine tool based on optimization with genetic algorithm. Robotics and Computer-Integrated . Manufacturing **75**, 102308 (2022). https://doi.org/10.1016/j.rcim.2021.102308

Shizhao Zhou received the B.Eng. degree in naval architecture and marine engineering in 2018 from Zhejiang University, Hangzhou, China, where he is currently working toward the Ph.D. degree in marine technology and engineering.

Chong Shen received the B.Eng. degree in ocean engineering in 2021 from Zhejiang University, Hangzhou, China, where he is currently working toward the master degree in electronic information engineering.

Fengye Pang received the B.Eng. degree in automation in 2020 from Nanc hang University, Nanchang, China. And he is currently working toward the master degree in electronic information engineering in Zhejiang University.

Zheng Chen received the B.Eng. and Ph.D. degrees in mechatronic control engineering from Zhejiang University, Zhejiang, China, in 2007 and 2012.

From 2013 to 2015, he was a Postdoctoral Researcher with the Department of Mechanical Engineering, Dalhousie University, Halifax, NS, Canada. Then he joined in Ocean College of Zhejiang University, China in July 2015 and currently serves as a Full Professor here. His research focuses mainly on advanced control of robotic and mechatronic system (e.g., nonlinear adaptive robust control, motion control, trajectory planning, tele-robotics, hydraulic system, precision mechatronic system, soft actuator and robot, mobile manipulator, underwater robot).

Jason Gu received the B.Eng. degree in electrical engineering and information science from the University of Science and Technology of China, Hefei, China, in 1992, the master's degree in biomedical engineering from Shanghai Jiaotong University Shanghai, China, in 1995, and the Ph.D. degree in electrical and computer engineering from the University of Alberta, Edmonton, AB, Canada, in 2001. He is currently a Full Professor of electrical and computer engineering with Dalhousie University, Halifax, NS, Canada. He is also a Cross-Appointed Professor with the School of Biomedical Engineering for his multidisciplinary research work. His research areas include robotics, biomedical engineering, rehabilitation engineering, neural networks, and control. Dr. Gu is currently a Fellow of the Engineering Institute of Canada.

Shiqiang Zhu received the B.S. degree in mechanical engineering from Zhejiang University, Hangzhou, China, in 1988, the M.S. degree in mechatronic engineering from Beijing Institute of Technology, Beijing, China, in 1991, and the Ph.D. degree in mechanical engineering from Zhejiang University, in 1995. He became a faculty at Zhejiang University in 1995 and was promoted to the rank of Professor in 2001. He is also the Director of Zhejiang Laboratory. His research interests include robotics and mechatronics.

Affiliations

Shizhao Zhou[1,2,3] · **Chong Shen**[3] · **Fengye Pang**[3] · **Zheng Chen**[1,2,3] (iD) · **Jason Gu**[4,5] · **Shiqiang Zhu**[3,5]

Shizhao Zhou
zhoushizhao@zju.edu.cn

Chong Shen
22134037@zju.edu.cn

Fengye Pang
22034037@zju.edu.cn

Jason Gu
jason.gu@dal.ca

Shiqiang Zhu
sqzhu@zju.edu.cn

[1] State Key Laboratory of Fluid Power and Mechatronic Systems, Zhejiang University, Hangzhou, 310000, China

[2] Hainan Institute of Zhejiang University, Sanya, 572025, China

[3] Ocean College, Zhejiang University, Zhoushan, 316021, China

[4] Department of Electrical and Computer Engineering, Dalhousie University, Halifax, NS B3H 4R2, Canada

[5] Zhejiang Laboratory, Hangzhou, 310000, China